Article

Gasdermin D pore structure reveals preferential release of mature interleukin-1

https://doi.org/10.1038/s41586-021-03478-3

Received: 3 January 2020

Accepted: 19 March 2021

Published online: 21 April 2021

Check for updates

Shiyu Xia[1,2], Zhibin Zhang[1,3], Venkat Giri Magupalli[1,2], Juan Lorenzo Pablo[4,5], Ying Dong[1,2], Setu M. Vora[1,2], Longfei Wang[1,2], Tian-Min Fu[1,2,6,7], Matthew P. Jacobson[8], Anna Greka[4,5], Judy Lieberman[1,3], Jianbin Ruan[1,2,9]✉ & Hao Wu[1,2]✉

As organelles of the innate immune system, inflammasomes activate caspase-1 and other inflammatory caspases that cleave gasdermin D (GSDMD). Caspase-1 also cleaves inactive precursors of the interleukin (IL)-1 family to generate mature cytokines such as IL-1β and IL-18. Cleaved GSDMD forms transmembrane pores to enable the release of IL-1 and to drive cell lysis through pyroptosis[1–9]. Here we report cryo-electron microscopy structures of the pore and the prepore of GSDMD. These structures reveal the different conformations of the two states, as well as extensive membrane-binding elements including a hydrophobic anchor and three positively charged patches. The GSDMD pore conduit is predominantly negatively charged. By contrast, IL-1 precursors have an acidic domain that is proteolytically removed by caspase-1[10]. When permeabilized by GSDMD pores, unlysed liposomes release positively charged and neutral cargoes faster than negatively charged cargoes of similar sizes, and the pores favour the passage of IL-1β and IL-18 over that of their precursors. Consistent with these findings, living—but not pyroptotic—macrophages preferentially release mature IL-1β upon perforation by GSDMD. Mutation of the acidic residues of GSDMD compromises this preference, hindering intracellular retention of the precursor and secretion of the mature cytokine. The GSDMD pore therefore mediates IL-1 release by electrostatic filtering, which suggests the importance of charge in addition to size in the transport of cargoes across this large channel.

Proteins of the gasdermin (GSDM) family are implicated in many inflammatory diseases and in cancer, and represent promising therapeutic targets[11]. GSDMs have a functional N-terminal fragment (NT) and an autoinhibitory C-terminal fragment (CT). Processing of GSDMs at the NT–CT linker by inflammatory caspases and other enzymes[12–17] liberates GSDM-NT for pore formation[3–6]. GSDMD pores mediate the release of cytokines of the IL-1 family[7,8] as well as programmed cell death, including pyroptosis[3–6,17–19]. However, despite the functional importance of GSDMD, the mechanisms of GSDMD pore formation and the role of the pore as an IL-1 secretion conduit are yet to be elucidated.

Structures of the GSDMD pore and prepore

We optimized human GSDMD samples by replacing a 17-residue segment between GSDMD-NT and GSDMD-CT with the 3C protease site; using phosphatidic acid (PA)-containing liposomes; solubilizing the pores in $C_{12}E_8$ detergent (C_x, x carbons in the alkyl chain; E_y, y ethylene glycol repeats); and further purifying by size-exclusion chromatography (Extended Data Fig. 1a–h). Because the 3C site does not affect pore formation[3], we denoted this construct as wild-type for simplicity. Further screening of mutant proteins[3,20] identified that GSDMD(L192E), which contains a leucine-to-glutamic acid mutation at residue 192, showed less aggregation and a reduced orientation preference on cryo-electron microscopy (cryo-EM) grids compared with the wild-type protein (Extended Data Figs. 1c–e, 2, 3a, b). Cryo-EM datasets from both wild-type GSDMD and GSDMD(L192E) yielded similar densities representative of β-barrel pores and rings without the β-barrel or prepores (Extended Data Fig. 3c). Models were built into the pore and the prepore densities of the L192E mutant, which had resolutions of 3.9 Å and 6.9 Å, respectively, measured using a Fourier shell correlation (FSC) cutoff of 0.143 (Extended Data Fig. 4, Extended Data Table 1).

GSDMD assemblies have 31-fold to 34-fold symmetry (Extended Data Figs. 2b, 3b). This is in contrast to the 26-fold to 28-fold symmetry[20] of GSDMA3, which suggests variability in oligomerization between different GSDMs as well as a modest size plasticity of a given GSDM. The 33-subunit GSDMD pore has inner and outer diameters of around 215 Å and 310 Å, respectively, which are 10–20% larger than those of the 27-subunit GSDMA3 pore (180 Å and 280 Å)[20] (Fig. 1a). This difference is independent of the acidic lipid in the liposomes and the detergent used for pore extraction (Extended Data Fig. 1i).

[1]Program in Cellular and Molecular Medicine, Boston Children's Hospital, Boston, MA, USA. [2]Department of Biological Chemistry and Molecular Pharmacology, Harvard Medical School, Boston, MA, USA. [3]Department of Pediatrics, Harvard Medical School, Boston, MA, USA. [4]Department of Medicine, Brigham and Women's Hospital, Boston, MA, USA. [5]Broad Institute of MIT and Harvard, Cambridge, MA, USA. [6]Department of Biological Chemistry and Pharmacology, The Ohio State University, Columbus, OH, USA. [7]The Ohio State University Comprehensive Cancer Center, Columbus, OH, USA. [8]Department of Pharmaceutical Chemistry, School of Pharmacy, University of California San Francisco, San Francisco, CA, USA. [9]Department of Immunology, University of Connecticut Health Center, Farmington, CT, USA. ✉e-mail: ruan@uchc.edu; wu@crystal.harvard.edu

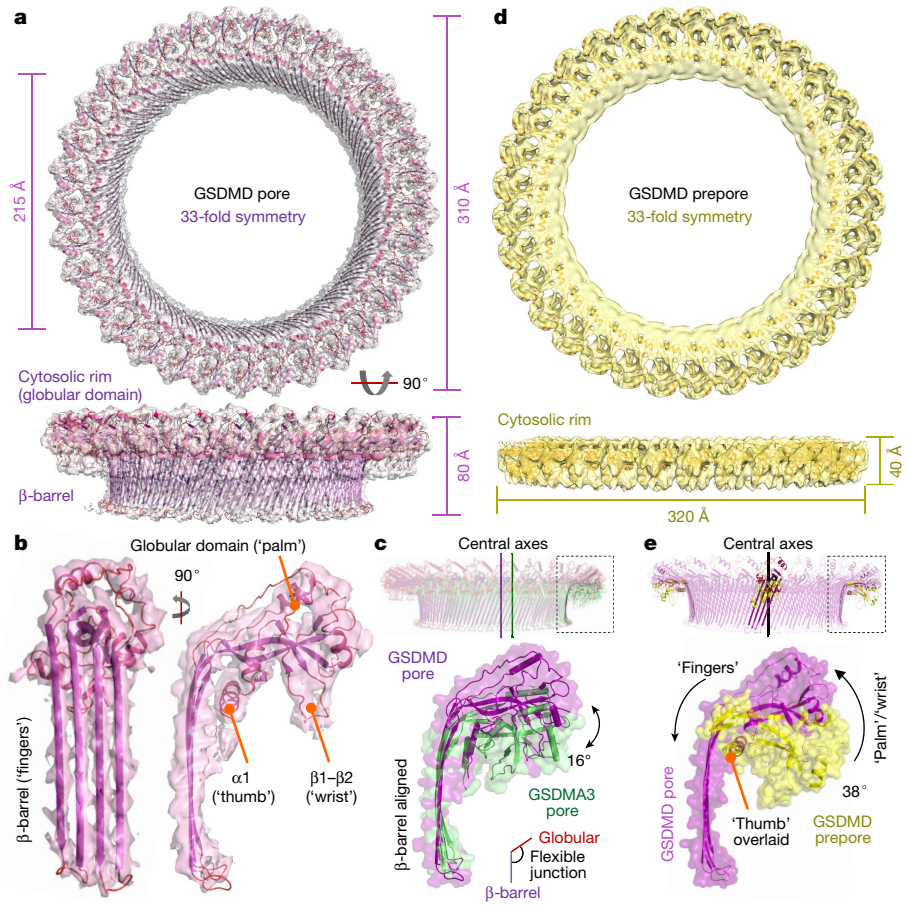

Fig. 1 | GSDMD architecture and conformational changes. a, Ribbon diagram and dimensions of the 33-subunit human GSDMD pore structure fitted into its cryo-EM density. The pore features a large transmembrane β-barrel and a globular domain on the cytosolic side. **b**, Structure of the pore-form GSDMD subunit fitted into the cryo-EM density. The structure resembles a human left hand, with the globular domain as the 'palm', the α1 helix as the 'thumb', the membrane-inserted β-hairpins as the 'fingers' and the β1–β2 loop as the 'wrist'. **c**, Flexible junction between the globular domain and the β-barrel, revealed by alignment of GSDMD and GSDMA3 pores at the β-barrel. The central axes are misaligned owing to the different pore sizes. The globular domain of the GSDMD pore is more membrane-distal than that of GSDMA3 by approximately 16°. **d**, Ribbon diagram and dimensions of the 33-subunit GSDMD prepore structure superimposed with its cryo-EM density. **e**, Prepore-to-pore transition of a GSDMD subunit. The two structures are aligned by their central axes and overlaid at the α1 helices. As the β-strands insert into the membrane, the globular domain rotates away from the membrane by approximately 38°.

Similar to in GSDMA3, each pore-form GSDMD subunit comprises two inserted β-hairpins ('fingers') and a globular domain ('palm') (Fig. 1b). However, there is a roughly 16° angle between the globular domain of pore-form GSDMD and that of GSDMA3, which suggests a flexible junction between the β-barrel and the globular domain (Fig. 1c).

The GSDMD prepore is 40 Å shorter in height than the pore (Fig. 1a, d). Prepore subunits resemble autoinhibited GSDMD-NT, which is globular, and the globular domain is preserved during pore formation (Extended Data Fig. 5a). However, the globular domain undergoes a 38° rigid-body rotation away from the membrane during pore formation, which can be visualized by aligning the pore and prepore by their central axes and the α1 helix or 'thumb' (Fig. 1e, Supplementary Video 1, 2). The inward rotation renders the pore slightly smaller in diameter than the prepore (Fig. 1a, d). Meanwhile, residues in extension domains 1 and 2 (ED1 and ED2) form the β-sheet by refolding into β-hairpins 1 and 2 (HP1 and HP2) (Extended Data Fig. 5b, c). GSDMA3 undergoes a similar rigid-body rotation (Extended Data Fig. 5d), which suggests structural conservation of the prepore-to-pore transition in GSDMs. As well as the prepore, other structural intermediates—such as arc- and slit-shaped oligomers, which have been observed under atomic force microscopy[6,21]—are also possible. The exact mechanism of GSDMD assembly in cells remains unknown.

Membrane contact sites

Analysis of the GSDMA3 pore identified the positively charged α1 helix (basic patch 1, denoted BP1) as being critical for interaction with acidic lipids[20]. However, in the case of GSDMD, the structure of the prepore suggested the involvement of a more membrane-proximal motif—the β1–β2 loop, which features a hydrophobic tip flanked by basic residues ('wrist', basic patch 2 (BP2)) (Figs. 1b, 2a). This loop remains ordered in the pore (Fig. 2b). We propose that the hydrophobic tip partially inserts into the lipid bilayer as an anchor, while the surrounding basic residues interact with acidic lipids. Liposome-based terbium (Tb^{3+}) leakage assays showed that membrane-permeabilization ability was compromised in the W48E and W50E mutants of human GSDMD (Extended Data Fig. 6a), and a double mutant (F50G/W51G) involving the equivalent residues in mouse GSDMD was defective in pore formation[22], confirming the importance of the anchor. The hydrophobic tip is conserved among GSDMs in terms of both sequence and structure (Extended Data Fig. 6b–d). Consistent with this, pore formation was reduced in the L47E and W49E mutants of GSDMA3, and was abolished in the case of the triple mutant L47E/F48E/W49E (Extended Data Fig. 6e).

Although BP1 and BP2 are highly conserved (Extended Data Fig. 6b) and are both located in the globular domain, there is a less-conserved basic patch (BP3) on the β7–β8 hairpin of the GSDMD pore subunit (Fig. 2c). The observation of density adjacent to BP3 that is potentially attributed to bound lipids supports the involvement of BP3 in membrane interaction (Extended Data Fig. 6f). To validate the roles of BP2 and BP3 in GSDMD, we generated the quadruple mutant GSDMD(R42E/K43E/K51E/R53E), which features mutations in BP2, and the single mutants GSDMD(R174E) and GSDMD(K204E), which involve residues of BP3. Pore formation was compromised in all mutants, and was eliminated entirely in the BP2 mutant (Extended Data Fig. 6g). Likewise, in GSDMA3, a quadruple mutation in BP2 (GSDMA3(R41E/K42E/R43E/K44E)) resulted in a loss of function (Extended Data Fig. 6h).

Full-length GSDMs do not bind lipids[3,22], and therefore the membrane contact sites are expected to be protected in autoinhibited GSDMs. After cleavage of the interdomain linker, GSDM-NT and GSDM-CT remain associated as a non-covalent complex in the absence of lipids[3]. On the basis of the structure of autoinhibited GSDMD, residues 242–283 of the interdomain linker are disordered[22]. Because

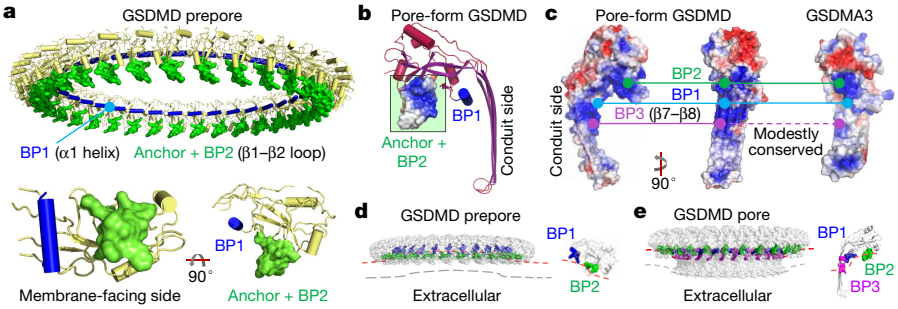

Fig. 2 | Membrane interaction by multiple contact sites. a, Membrane docking by the β1–β2 loop, the most membrane-proximal feature of the prepore. The loop contains a hydrophobic anchor flanked by basic residues of BP2. The relative positions of BP1 and the anchor + BP2 region are displayed using an individual prepore subunit in two orientations. **b**, Pore-form GSDMD with the hydrophobic anchor and BP2 boxed in green and the local electrostatic surface shown. **c**, Locations and conservation of the three BPs in GSDMD, at the α1, β1–β2 (excluding the hydrophobic tip) and β7–β8 regions, respectively. Continuous lines indicate conserved; a dashed line indicates that BP3 is modestly conserved. **d**, **e**, Potential membrane distortion around the GSDMD prepore (**d**) and the pore (**e**). A subunit of each is enlarged to show the inferred local curvature. The contrasting curvatures indicate convexity-to-concavity membrane remodelling.

residues Q241 and T284 are located near the β1–β2 loop (anchor and BP2), it is possible that the linker hovers over and masks the loop. Cleavage of the linker could therefore unmask the β1–β2 loop for lipid interaction (Extended Data Fig. 6i). It is therefore likely that the β1–β2 loop is the initial membrane-engagement site. Furthermore, if the basic patches co-interact with acidic lipids, the membrane would be convex (curved towards the cytosol) next to the GSDMD prepore and concave (curved towards the extracellular space) next to the pore (Fig. 2d, e). Notably, GSDMD-perforated membranes can be repaired by the ESCRT-III machinery[23], which assembles favourably on concave membranes[24]. It is therefore likely that, by pore formation, GSDMD primes its own removal from the membrane through negative feedback.

Predominantly acidic conduit

Electrostatic calculations revealed that negative potentials originate from the globular domain and the β-barrel and decay towards the centre of the GSDMD pore (Fig. 3a, b). There are four solvent-exposed acidic patches (APs) near the conduit (Fig. 3a, Extended Data Fig. 7a): AP1 (β2–β3, containing five D or E residues) and AP4 (β11, 4 D) in the globular domain, and AP2 (β3, 2 D/E) and AP3 (β7, 3 E) in the β-barrel (Fig. 3a). As with GSDMD, the GSDMA3 pore conduit is also predominantly acidic (AP1 and AP2 of GSDMA3 have 4 D/E and 2 D/E, respectively) (Fig. 3a). AP1 and AP2 mutants were generated by the mutation of D or E residues to alanines; these mutants showed equivalent functionality and pore size compared with wild-type GSDMD or GSDMA3

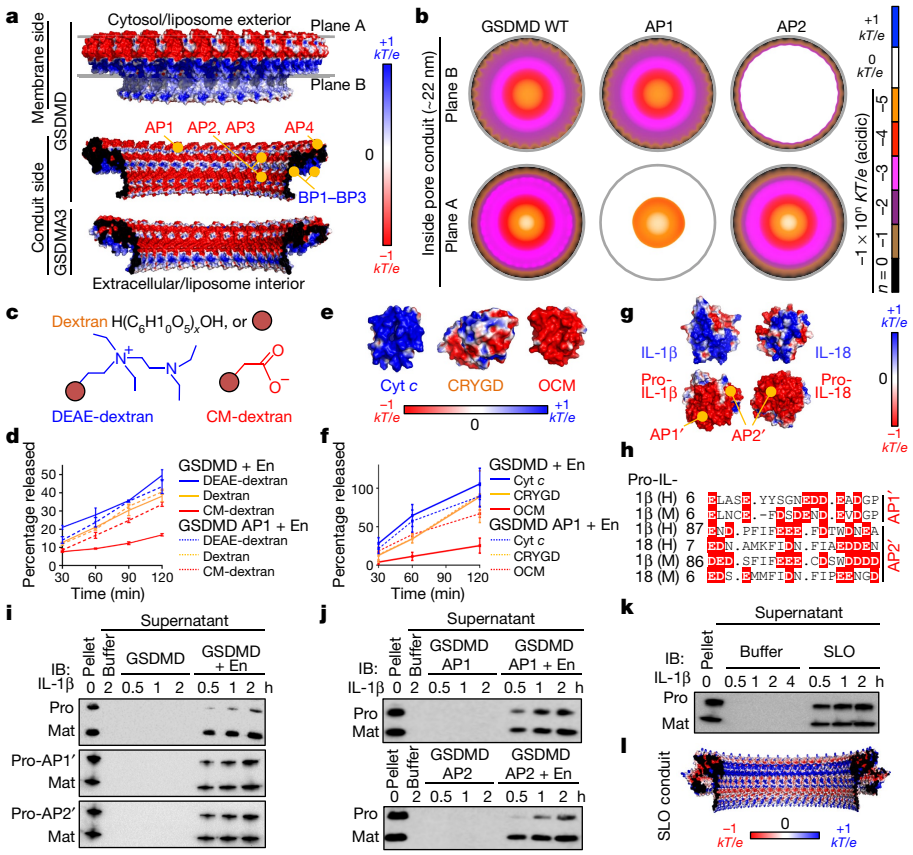

Fig. 3 | Pore conduit and cargo transport. **a**, Electrostatic surface (−1 to +1 *kT/e*) of the GSDMD pore, with the membrane-bound side formed by BPs and the solvent-exposed side formed by APs. The GSDMA3 pore conduit is similarly acidic. **b**, Negative electrostatic coverage of the GSDMD pore conduit. Modelled AP1 (5 D/E to A) and AP2 (2 D/E to A) pores have locally neutral conduits. **c**, **d**, Schematics of dextran cargoes (**c**) and their release from liposomes perforated by GSDMD, quantified by fluorescein isothiocyanate (FITC) fluorescence ($n = 3$ biological replicates) (**d**). En, activating enzyme. **e**, **f**, Electrostatic surfaces of three protein cargoes (cyt *c*, CRYGD and OCM; Protein Data Bank (PDB) IDs 2B4Z, 1H4A and 1TTX, respectively) (**e**) and their release from liposomes permeabilized by GSDMD, evaluated by immunoblotting ($n = 3$ biological replicates) (**f**). **g**, Basification of IL-1β and IL-18 through caspase-1-induced maturation. **h**, APs of the IL-1β and IL-18 precursors shown by aligned sequences. H, human; M, mouse. Dashes indicate gaps and dots indicate strings of omitted residues. **i**, **j**, Release of pro- (wild-type and AP′-mutant) and mature (mat) IL-1β from liposomes permeabilized by wild-type GSDMD (**i**) and the reciprocal experiments (**j**). IB, immunoblot. Pro-AP1′: 8 D/E to K; Pro-AP2′: 11 D/E to K. **k**, Release of pro- and mature IL-1β from liposomes perforated by SLO. **l**, Electrostatic surface of the modelled SLO pore conduit. Data shown in **d**, **f** are mean ± s.d. Data shown in **i**–**k** are representative of two independent experiments.

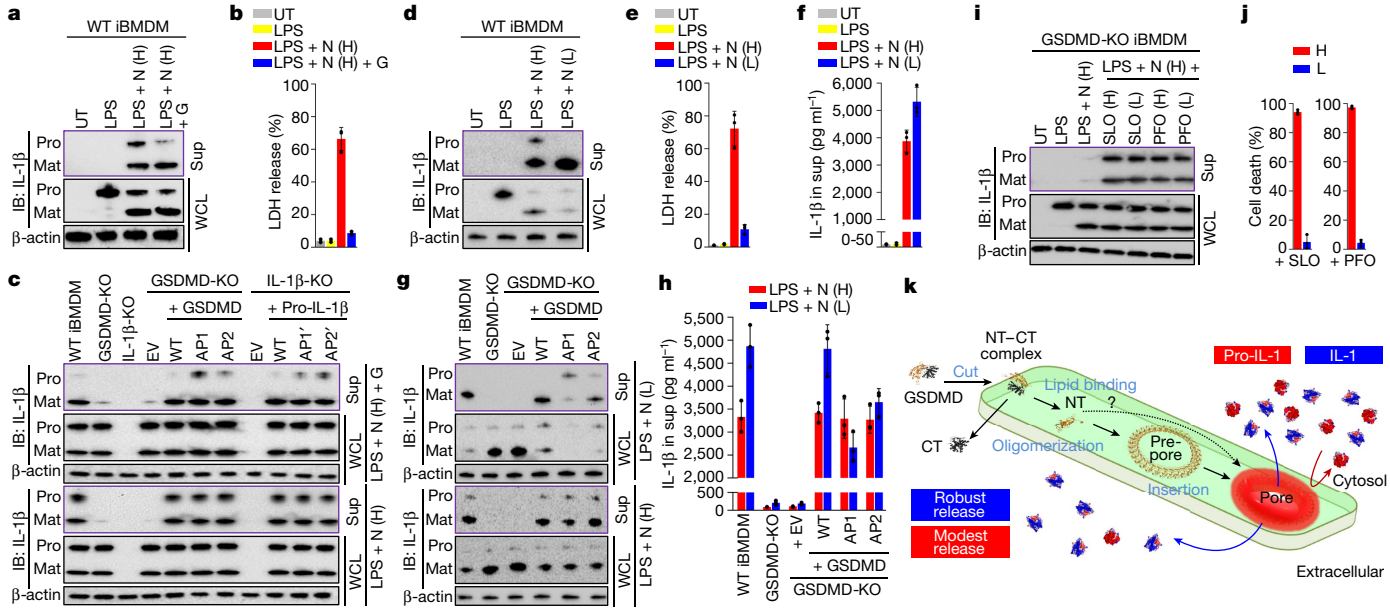

Fig. 4 | Preferential IL-1β release from macrophages. a, **b**, Preferential release of mature IL-1β from glycine-protected living iBMDMs permeabilized by GSDMD, shown by immunoblotting (**a**) and LDH release ($n = 3$ biological replicates) (**b**). UT, untreated; N, nigericin; G, glycine; H, high dose (20 μM); LPS, lipopolysaccharide; Sup, supernatant; WCL, whole-cell lysate. **c**, Comparison of IL-1β release across GSDMD-knockout iBMDMs expressing wild-type or AP-mutant GSDMD, and across pro-IL-1β-knockout iBMDMs expressing wild-type or AP′-mutant pro-IL-1β. EV, empty vector, a mock transduction control. **d**–**f**, Release of mature IL-1β from living iBMDMs without glycine protection, characterized by immunoblotting (**d**), LDH release ($n = 3$ biological replicates) (**e**) and ELISA ($n = 3$ biological replicates) (**f**). L, low dose (0.5 μM). **g**, **h**, Comparison of IL-1β release across GSDMD-knockout iBMDMs expressing wild-type or AP-mutant GSDMD without glycine protection, evaluated by immunoblotting (**g**) and ELISA ($n = 3$ biological replicates) (**h**). **i**, **j**, Comparable leakage of pro-IL-1β and mature IL-1β from GSDMD-knockout iBMDMs perforated by SLO and PFO (**i**) at cytotoxic and non-toxic concentrations shown by ATP-based cell death ($n = 3$ biological replicates) (**j**). H, high dose (625 nM); L, low dose (0.16 nM). **k**, Schematic of GSDMD pore formation and IL-1 release. The question mark indicates other possible assembly mechanisms. Data shown in **b**, **e**, **f**, **h** and **j** are mean ± s.d. Data are representative of three (**a**, **d**) or two (**c**, **g**, **i**) independent experiments.

(Extended Data Fig. 7b–e). In terms of electrostatics, mutations in AP1 and AP2 locally diminish the negative potentials in the cargo release path (Fig. 3a, b).

It has previously been shown that a size-exclusion mechanism allows small charge-neutral dextrans—but not large ones—to exit from GSDMD-permeabilized liposomes[7]. Because soluble cargoes may possess a charged surface, we tested whether the acidic conduit of the GSDMD pore influences cargo transport. It is notable that, although pores formed by GSDMD subunits outside of liposomes have a reversed geometry compared with those formed inside cells, cargo released in either case would experience an equivalent total electrostatic interaction along the trajectory (Fig. 3a, b). Using a sub-lytic concentration of GSDMD—which induced liposome permeabilization but not lysis, as confirmed by minimal lactate dehydrogenase (LDH) release (Extended Data Fig. 8a)—we found that small dextrans (40 kDa) carrying different charges (neutral unmodified, basic diethylaminoethyl (DEAE)-modified, and acidic carboxymethyl (CM)-modified) were released to various extents, of which CM-dextran was the lowest (Fig. 3c, d). Use of the AP1 mutant of GSDMD resulted in markedly enhanced release of CM-dextran, and had only a minimal effect on the release of the neutral and basic counterparts (Fig. 3d). We then examined three small proteins—cytochrome *c* (cyt *c*) (basic), γ-crystallin D (CRYGD) (neutral) and oncomodulin (OCM) (acidic)—that have similar hydrated diameters but contrasting surface electrostatics (Fig. 3e). Consistent with the above results, OCM was released most slowly from unlysed liposomes through GSDMD pores, and the AP1 mutant abolished this retardation effect (Fig. 3f, Extended Data Fig. 8b). Release rates of the basic and neutral dextrans, and of cyt *c* and CRYGD, showed no notable differences with wild-type and mutant GSDMD. Therefore, the GSDMD pore repels acidic cargoes but does not seem to robustly favour basic over neutral cargoes. These observations could help to explain the rapid, GSDMD-dependent release of Rac-1, HMGB1 and cyt *c*, all of which are non-acidic[8,25,26].

A prominent biological role of the GSDMD pore is to mediate the unconventional secretion[7,8] of IL-1β and IL-18, which are cytokines of the IL-1 family that lack the signal sequence required for endoplasmic reticulum- and Golgi-dependent secretion. Precursor (pro) and mature IL-1β and IL-18 are similar in size and are both much smaller than the GSDMD pore; notably, these cytokines basify during proteolytic maturation (Fig. 3g, h). Basic, mature IL-1β has been reported to accumulate at phosphatidylinositol-4,5-bisphosphate (PtdIns(4,5)P_2) ruffles on the cell membrane before secretion[10]. To eliminate the potential effects of binding to PtdIns(4,5)P_2, we encapsulated pro- and mature IL-1β and IL-18 into PtdIns(4,5)P_2-free liposomes to study their GSDMD-dependent release (Extended Data Fig. 8c). Mature IL-1β and IL-18 were secreted considerably faster than their precursors (Fig. 3i, Extended Data Fig. 8d, e, Supplementary Fig. 1)—as if the pore acts as a 'filter' to repel the precursors. Indeed, AP1 and AP2 mutants of both GSDMD and GSDMA3 enhanced the release of pro-IL-1β (Fig. 3i, j, Extended Data Fig. 8f, g), an effect that may be rationalized as a result of decreased repulsion along part of the cargo trajectory (Fig. 3b). Reciprocally, the AP1′ (8 D/E to K) and AP2′ (11 D/E to K) mutants of pro-IL-1β were released at higher rates than wild-type pro-IL-1β (Fig. 3i). Using a simplified mathematical relationship, we estimated that the electrostatic potential of the GSDMD pore conduit needs to be around −0.15 kT/e (in which k is the Boltzmann constant, T is the temperature and e is the elementary charge) on average to account for the observed charge effect (Extended Data Fig. 8h–k)—a value that is within the range deduced structurally (Fig. 3a, b). To further confirm that the differences in release rates are attributed to the GSDM pores, we tested the release

of cargo from liposomes permeabilized by the β-barrel-forming toxins streptolysin O (SLO) and perfringolysin O (PFO). Under a sub-lytic condition (confirmed by a lack of release of a bulky 2 MDa dextran from liposomes), SLO and PFO did not induce the preferential release of mature IL-1β (Fig. 3k, Extended Data Fig. 8l, m). Consistent with this, SLO and PFO pore conduits are neither predominantly acidic nor basic according to homology models based on the structure of pneumolysin[27] (Fig. 3l, Extended Data Fig. 8n).

Electrostatically filtered IL-1 release

GSDMD-dependent IL-1 release can occur independently of pyroptosis, as evidenced by treatment with glycine that inhibited cell membrane rupture but still enabled the release of IL-1β but not LDH (a hallmark of pyroptosis)[7,8]. In light of the minimal release of pro-IL-1β in the liposome experiments, we asked whether this phenomenon could be observed in cells. We found that, whereas mature IL-1β was readily secreted from immortalized mouse bone-marrow-derived macrophages (iBMDMs) with (induced by 20 μM nigericin for 30 min) or without (glycine-protected) pyroptosis, pro-IL-1β was largely retained in living but not in pyroptotic cells (Fig. 4a, b). To further assess whether the GSDMD pore directly influences the release of IL-1β, we expressed comparable levels of wild-type, AP1-mutant or AP2-mutant GSDMD in GSDMD-knockout iBMDMs, and wild-type, AP1′-mutant or AP2′-mutant pro-IL-1β in IL-1β-knockout iBMDMs (Extended Data Fig. 9a). All cells except the knockout and empty-vector controls were prone to nigericin-induced pyroptosis and were protected by glycine (Extended Data Fig. 9b). In comparison with wild-type iBMDMs, cells expressing AP1- or AP2-mutant GSDMD, or AP1′- or AP2′-mutant pro-IL-1β, showed enhanced release of pro-IL-1β under glycine protection (Fig. 4c).

Given that pro-IL-1β is inactive and is unable to bind to the IL-1 receptor, we postulated that the GSDMD pore retains pro-IL-1β for processing to achieve sustained secretion of mature IL-1β. To test this hypothesis, we weakly stimulated the iBMDMs with low-dose nigericin (0.5 μM) to enable sustained IL-1β secretion with little cell death (12 h), in the absence of the osmoprotectant glycine (Fig. 4d, e). The amount of mature IL-1β secreted was greater after treatment with low-dose nigericin than high-dose nigericin, probably due to minimal pyroptosis and continuous IL-1β release (Fig. 4f). Under the weaker stimulation, cells expressing the AP1 and AP2 GSDMD mutants not only released pro-IL-1β as did pyroptotic cells, but also secreted markedly lower amounts of mature IL-1β than did cells expressing wild-type GSDMD (Fig. 4g, h, Extended Data Fig. 9c). Therefore, by electrostatically impeding the release of pro-IL-1β, the GSDMD pore plays an important part in sustained IL-1β secretion from living cells. Furthermore, we expressed a caspase-1-cleavable GSDMA3 chimera (A3chim) and its equivalent AP mutants in GSDMD-knockout iBMDMs (Extended Data Fig. 9d, e) and found that GSDMA3 also invokes this charge-based mechanism (Extended Data Fig. 9f–o). By contrast, SLO and PFO induced similar levels of secretion of pro-IL-1β and IL-1β from GSDMD-knockout iBMDMs with or without cell death (Fig. 4i, j), as was observed in the liposome experiments (Fig. 3k, Extended Data Fig. 8l, m).

In summary, the structures we describe here provide mechanistic insights into the formation of the GSDMD pore and the preferential release of mature IL-1 (Fig. 4k). It remains uncertain whether IL-1α uses the GSDMD pore conduit as a major secretion pathway. Because both pro- and mature IL-1α are acidic, the pore may deter—if not abolish—their passage. Supporting this suggestion, previous studies have demonstrated a distinct secretory route for IL-1α[28,29] and a lack of secretion under glycine protection[30]. Additionally, it is likely that charge endows GSDM pores with differential electrostatics to fine-tune the exit of damage-associated molecular patterns. Finally, although electrostatics modulate cargo transport, they might not provide absolute gating given the large sizes of GSDM pores. Alternative mechanisms that contribute to the release of damage-associated molecular patterns from GSDM-perforated living cells remain to be discovered.

Online content

Any methods, additional references, Nature Research reporting summaries, source data, extended data, supplementary information, acknowledgements, peer review information; details of author contributions and competing interests; and statements of data and code availability are available at https://doi.org/10.1038/s41586-021-03478-3.

1. Kayagaki, N. et al. Caspase-11 cleaves gasdermin D for non-canonical inflammasome signalling. *Nature* **526**, 666–671 (2015).
2. Shi, J. et al. Cleavage of GSDMD by inflammatory caspases determines pyroptotic cell death. *Nature* **526**, 660–665 (2015).
3. Ding, J. et al. Pore-forming activity and structural autoinhibition of the gasdermin family. *Nature* **535**, 111–116 (2016).
4. Liu, X. et al. Inflammasome-activated gasdermin D causes pyroptosis by forming membrane pores. *Nature* **535**, 153–158 (2016).
5. Aglietti, R. A. et al. GsdmD p30 elicited by caspase-11 during pyroptosis forms pores in membranes. *Proc. Natl Acad. Sci. USA* **113**, 7858–7863 (2016).
6. Sborgi, L. et al. GSDMD membrane pore formation constitutes the mechanism of pyroptotic cell death. *EMBO J.* **35**, 1766–1778 (2016).
7. Evavold, C. L. et al. The pore-forming protein gasdermin D regulates interleukin-1 secretion from living macrophages. *Immunity* **48**, 35–44.e6 (2018).
8. Heilig, R. et al. The gasdermin-D pore acts as a conduit for IL-1β secretion in mice. *Eur. J. Immunol.* **48**, 584–592 (2018).
9. Kayagaki, N. et al. NINJ1 mediates plasma membrane rupture during lytic cell death. *Nature* **591**, 131–136 (2021).
10. Monteleone, M. et al. Interleukin-1β maturation triggers its relocation to the plasma membrane for gasdermin-D-dependent and -independent secretion. *Cell Rep.* **24**, 1425–1433 (2018).
11. Liu, X., Xia, S., Zhang, Z., Wu, H. & Lieberman, J. Channelling inflammation: gasdermins in physiology and disease. *Nat. Rev. Drug Discov.* (2021).
12. Orning, P. et al. Pathogen blockade of TAK1 triggers caspase-8-dependent cleavage of gasdermin D and cell death. *Science* **362**, 1064–1069 (2018).
13. Sarhan, J. et al. Caspase-8 induces cleavage of gasdermin D to elicit pyroptosis during *Yersinia* infection. *Proc. Natl Acad. Sci. USA* **115**, E10888–E10897 (2018).
14. Burgener, S. S. et al. Cathepsin G inhibition by Serpinb1 and Serpinb6 prevents programmed necrosis in neutrophils and monocytes and reduces GSDMD-driven inflammation. *Cell Rep.* **27**, 3646–3656.e5 (2019).
15. Zhang, Z. et al. Gasdermin E suppresses tumour growth by activating anti-tumour immunity. *Nature* **579**, 415–420 (2020).
16. Zhou, Z. et al. Granzyme A from cytotoxic lymphocytes cleaves GSDMB to trigger pyroptosis in target cells. *Science* **368**, eaaz7548 (2020).
17. Sollberger, G. et al. Gasdermin D plays a vital role in the generation of neutrophil extracellular traps. *Sci. Immunol.* **3**, eaar6689 (2018).
18. Wang, Q. et al. A bioorthogonal system reveals antitumour immune function of pyroptosis. *Nature* **579**, 421–426 (2020).
19. Chen, K. W. et al. Noncanonical inflammasome signaling elicits gasdermin D-dependent neutrophil extracellular traps. *Sci. Immunol.* **3**, eaar6676 (2018).
20. Ruan, J., Xia, S., Liu, X., Lieberman, J. & Wu, H. Cryo-EM structure of the gasdermin A3 membrane pore. *Nature* **557**, 62–67 (2018).
21. Mulvihill, E. et al. Mechanism of membrane pore formation by human gasdermin-D. *EMBO J.* **37**, e98321 (2018).
22. Liu, Z. et al. Crystal structures of the full-length murine and human gasdermin D reveal mechanisms of autoinhibition, lipid binding, and oligomerization. *Immunity* **51**, 43–49.e4 (2019).
23. Rühl, S. et al. ESCRT-dependent membrane repair negatively regulates pyroptosis downstream of GSDMD activation. *Science* **362**, 956–960 (2018).
24. Lee, I. H., Kai, H., Carlson, L. A., Groves, J. T. & Hurley, J. H. Negative membrane curvature catalyzes nucleation of endosomal sorting complex required for transport (ESCRT)-III assembly. *Proc. Natl Acad. Sci. USA* **112**, 15892–15897 (2015).
25. Davis, M. A. et al. Calpain drives pyroptotic vimentin cleavage, intermediate filament loss, and cell rupture that mediates immunostimulation. *Proc. Natl Acad. Sci. USA* **116**, 5061–5070 (2019).
26. Rogers, C. et al. Gasdermin pores permeabilize mitochondria to augment caspase-3 activation during apoptosis and inflammasome activation. *Nat. Commun.* **10**, 1689 (2019).
27. van Pee, K. et al. CryoEM structures of membrane pore and prepore complex reveal cytolytic mechanism of Pneumolysin. *eLife* **6**, e23644 (2017).
28. Tapia, V. S. et al. The three cytokines IL-1β, IL-18, and IL-1α share related but distinct secretory routes. *J. Biol. Chem.* **294**, 8325–8335 (2019).
29. Martín-Sánchez, F. et al. Inflammasome-dependent IL-1β release depends upon membrane permeabilisation. *Cell Death Differ.* **23**, 1219–1231 (2016).
30. Batista, S. J. et al. Gasdermin-D-dependent IL-1α release from microglia promotes protective immunity during chronic *Toxoplasma gondii* infection. *Nat. Commun.* **11**, 3687 (2020).

Methods

Data reporting

No statistical methods were used to predetermine sample size. The experiments were not randomized and the investigators were not blinded to allocation during experiments and outcome assessment.

Generation of full-length GSDMs

The coding sequence of full-length human GSDMD was cloned into the pDB.His.MBP vector after the N-terminal His_6-maltose binding protein (MBP) tag and a linker cleavable by tobacco etch virus (TEV) protease. Residues 259–275 (between GSDMD-NT (residues 1–241) and GSDMD-CT (residues 284–484)) were then replaced by the human rhinovirus 3C protease (3C) site (LEVLFQ/GP). As this construct does not contain a mutation in GSDMD-NT, we designate it 'wild-type GSDMD' for brevity, and all mutants were generated on this background. All mutations in this study were introduced using the QuikChange Site-Directed Mutagenesis Kit (Stratagene) or Gibson Assembly Master Mix (New England BioLabs), and all plasmids were verified by sequencing. Transformed *Escherichia coli* BL21 (DE3) cells were grown in LB medium supplemented with 50 μg ml^{-1} kanamycin at 37 °C, induced at an optical density at 600 nm (OD_{600}) of 0.6 by 0.5 mM isopropyl β-D-1-thiogalactopyranoside (IPTG), and incubated for 18 h at 18 °C before collection. Cells were pelleted by centrifugation at 2,990*g* for 30 min and resuspended in buffer A (40 mM HEPES at pH 7.0, 150 mM NaCl) supplemented with 5 mM imidazole for lysis by sonication. His_6-MBP-tagged GSDMD was enriched on Ni-NTA beads (Qiagen) and eluted by buffer A supplemented with 500 mM imidazole. For reconstitution of the GSDMD pore and prepore, the His_6-MBP tag was cleaved by His_6-TEV at 4 °C overnight. His_6-MBP and His_6-TEV were removed using a Ni-NTA column and the flow-through containing GSDMD was further purified using a Superdex 200 (10/300) size-exclusion column (GE Healthcare Life Sciences) equilibrated with buffer A. Engineered mouse GSDMA3 containing the 3C site, GSDMA3 chimeras and their mutants were cloned and purified following a previous protocol[20]. Suggestions on the design of caspase-1-cleavable GSDMA3 were provided by F. Shao. Three GSDMA3 chimeras were designed as follows: (1) A3chim: GSDMA3-NT (residues 1–240), followed by the linker of pro-IL-1β (residues 101–122), followed by GSDMA3-CT (residues 263–464); (2) A3chim2: GSDMA3-NT, followed by the linker of GSDMD (residues 266–287), followed by GSDMA3-CT; (3) A3chim3: GSDMA3-NT, followed by the linker of GSDMD, followed by GSDMD-CT (residues 288–487). The AP mutations were then introduced to A3chim. A3chim3 was poorly expressed and was not further evaluated. All purified full-length GSDMs were concentrated to approximately 10 mg ml^{-1} before use.

Reconstitution and purification of GSDMD and GSDMA3 assemblies

1,2-Dioleoyl-*sn*-glycero-3-phosphate (PA, in the case of GSDMD) or 1′,3′-bis[1,2-dioleoyl-*sn*-glycerol-3-phospho]-glycerol (CL, in the case of GSDMA3) was mixed with 1-palmitoyl-2-oleoyl-*sn*-glycero-3-phosphocholine (PC) (Avanti Polar Lipids) at a molar ratio of 1:4. Besides PA and CL, other acidic lipids such as 1,2-dioleoyl-*sn*-glycero-3-phospho-L-serine (PS) (Avanti Polar Lipids) were tested in combination with PC at various ratios including 1:4; however, these mixtures yielded suboptimal samples. The solvent chloroform was evaporated under nitrogen gas and resuspended in buffer A to a lipid concentration of approximately 5 mM by vigorous vortexing. The liposomes formed were extruded through a 100 nm filter (Whatman Nuclepore) for 30 passes to generate unilamellar vesicles. Purified GSDMD was added at a final concentration of around 50 μM, followed by addition of ample 3C to cleave GSDMD for pore formation. The reaction proceeded on ice for 3 h before the liposomes loaded with GSDMD-NT pores were pelleted at 200,000*g* for 1 h in a cold ultracentrifuge. The supernatant containing mostly full-length GSDMD, GSDMD-CT and 3C was discarded, and the pellet was solubilized by buffer A supplemented with 1% C12E8 (Anatrace) to extract GSDMD assemblies. To remove aggregates, solubilized GSDMD samples were subject to fractionation using a Superose 6 (10/300) size-exclusion column (GE Healthcare Life Sciences) equilibrated with buffer A supplemented with 0.2% C12E8. GSDMA3 assemblies were reconstituted and purified following established procedures[20].

IL-1 purification

All IL-1-related liposomal experiments were conducted using pure, monomeric, tag-free, freshly purified precursor or mature IL-1β and IL-18. To obtain the IL-1 cargoes, coding sequences for full-length mouse pro-IL-1β and pro-IL-18, wild-type or charge-mutant, were inserted into a pET28a vector immediately after the N-terminal His_6-SUMO tag. Sequences coding the pro-domains of pro-IL-1β and pro-IL-18 (residues 1–117 and 1–35, respectively) were then truncated out to generate vectors expressing His_6-SUMO-tagged mature IL-1β and IL-18. Plasmids were transformed into *E. coli* BL21 (DE3) RipL cells for expression in LB medium supplemented with 50 μg ml^{-1} kanamycin. Protein expression was induced with 0.2 mM IPTG at an OD_{600} of 0.8. The culture was then incubated at 18 °C for 12 h under vigorous shaking. Pelleted cells were resuspended in buffer A for sonication, and lysates were incubated with Ni-NTA beads to enrich His_6-SUMO-tagged proteins. The His_6-SUMO tag was cleaved off on-column using His_6-tagged ULP1 protease overnight at 4 °C. The flow-through containing tag-free IL-1 proteins was further purified by gel filtration using the Superdex 75 (10/300) column (GE Healthcare Life Sciences) equilibrated with buffer A. Only fractions under the monomeric chromatograph peaks were collected and used directly without further concentration.

SLO and PFO purification

Sequences encoding SLO (residues 78–571) and PFO (residues 30–500) were cloned into a pET-28 vector to append an N-terminal His_6-tag. The plasmids were transformed into *E. coli* BL21 (DE3). Expression was induced by 1 mM IPTG at 37 °C at an OD_{600} of 1.0. The bacteria were incubated at 37 °C for 4 h under vigorous shaking before they were collected, resuspended in buffer A, and lysed by sonication. Proteins eluted from Ni-NTA beads by buffer A supplemented with 500 mM imidazole were further purified using a Superdex 200 (10/300) column (GE Healthcare Life Sciences) equilibrated with buffer A supplemented with 5 mM dithiothreitol (DTT). Fractions containing pure SLO or PFO were pooled and concentrated to approximately 10 mg ml^{-1} before use.

Caspase-1 purification

Human caspase-1 p20 (residues 120–297) and p10 (residues 317–404) subunits were individually cloned into the pET-21a vector and expressed in *E. coli* BL21 (DE3). Expression was induced with 1 mM IPTG for 4 h at 37 °C. Bacterial pellets were washed twice with buffer containing 50 mM Tris-HCl (pH 8.0), 300 mM NaCl, 0.1% Triton-X-100 and 1 M guanidinium hydrochloride (GdnCl), and insoluble contents were pelleted by centrifugation at 17,000*g* for 30 min. Inclusion bodies were collected and washed twice with buffer containing 50 mM Tris-HCl (pH 8.0), 300 mM NaCl and 1 M GdnCl, and then solubilized in buffer containing 6 M GdnCl, 25 mM Tris-HCl (pH 7.5), 5 mM EDTA and 100 mM tris(2-carboxyethyl) phosphine (TCEP). Approximately equal molar amounts of each subunit were mixed to a total volume of 6 ml and diluted into 250 ml of buffer containing 100 mM HEPES (pH 8.0), 100 mM NaCl, 100 mM sodium malonate, 20% sucrose, 0.5 M NDSB-201 and 10 mM TCEP. The refolded proteins were concentrated and dialysed overnight over buffer containing 30 mM sodium acetate (pH 5.9), 5 mM TCEP, 5% (v/v) glycerol, and then purified by HiTrap SP cation-exchange chromatography (GE Healthcare Life Sciences) with buffer containing 30 mM sodium acetate (pH 5.9), 1 M NaCl, 5 mM TCEP and 10% (v/v) glycerol. To test cleavage, approximately equimolar amounts of purified caspase-1 and full-length GSDMs were mixed and incubated on ice for 4 h before SDS–PAGE analysis.

Electron microscopy imaging and data processing

GSDM samples were checked for morphology and homogeneity using negative-staining electron microscopy. Samples (5 µl) were applied to glow-discharged Formvar-coated copper grids (Electron Microscopy Sciences), washed with 30 µl buffer A, stained with 1% uranyl formate for 30 s, and blotted dry. Imaging was performed on a Tecnai G^2 Spirit BioTWIN electron microscope (FEI) equipped with a 2k CCD camera (Advanced Microscopy Techniques) at the Electron Microscopy Facility at Harvard Medical School. For cryo-EM grid preparation, GSDMD samples (3 µl, 1–3 mg ml^{-1} protein concentration) were applied to plasma glow-discharged 300-mesh gold lacey carbon grids coated with ultrathin carbon film (Ted Pella), using a Vitrobot (FEI) set at blotting force 2, blotting time 7 s, 100% humidity and 4 °C. Blotted grids were immediately plunged into liquid ethane and transferred to liquid nitrogen for storage. Two cryo-EM datasets were collected using Titan Krios electron microscopes (FEI) equipped with K3 cameras (Gatan) and the SerialEM software: one dataset for wild-type GSDMD and the other for GSDMD(L192E) samples (Extended Data Table 1). Both datasets were processed in RELION 3.0[31]. Raw movies were corrected for beam-induced motion using MotionCor2[32], and per-micrograph defocus was determined using CTFFIND4[33]. Motion- and contrast transfer function (CTF)-corrected micrographs were examined manually to discard images of unsatisfactory quality. The GSDMD pores and prepores stacked double-ring particles, probably an artefact of detergent solubilization, and therefore all 3D reconstructions were conducted on density-subtracted single rings. Afterwards, CTF refinement was performed to determine per-particle defocus level. Local resolution distribution was determined using ResMap[34].

Model building and structure analysis

The wild-type GSDMD and the GSDMD(L192E) datasets yielded similar cryo-EM densities for both the pore and the prepore. The densities for GSDMD(L192E) at 3.9 Å (the 33-fold symmetric pore) and 6.9 Å (the 33-fold symmetric prepore) resolutions by gold-standard FSC (0.143) were used for model building. In building the pore model, the structure of GSDMD-NT in the autoinhibited state (PDB: 6N9O) was docked into the globular domain part of the pore map in UCSF Chimera[35]. Then, extensive manual remodelling of the β-barrel domain was performed in Coot[36]. The model was refined against the map in real space using PHENIX[37]. For the prepore model, 33 copies of the autoinhibited GSDMD-NT structure were fitted into the prepore map as rigid bodies. No manual remodelling or refinement was performed owing to limited resolution of the prepore map. Structural models of pro-IL-1β and pro-IL-18 were generated on the basis of crystal structures of IL-1β (PDB: 9ILB) and IL-18 (PDB: 3WO2), using the I-TASSER server[38]. Structural models of GSDMD AP1- and AP2-mutant pores were generated by in silico mutagenesis using the PyMOL Molecular Graphics System. Structural models of SLO and PFO pores were generated by the SWISS-MODEL server based on homology to pneumolysin (PDB: 5LY6). Values of electrostatic potentials at a physiological salt concentration of 150 mM and an aqueous dielectric constant of 78 were obtained using the Adaptive Poisson-Boltzmann Solver (APBS)[39] plugin in PyMOL. All structural representations were generated using UCSF Chimera and PyMOL.

Terbium release assay

Terbium (Tb^{3+}) liposome leakage assays were performed following an established protocol[40]. In brief, CL, 1-palmitoyl-2-oleoyl-*sn*-glycero-3-phosphoethanolamine (PE) and PC (Avanti Polar Lipids) were mixed at a mass ratio of 5:8:4. The solvent chloroform was evaporated under nitrogen gas and the lipids were resuspended in buffer B (20 mM HEPES at pH 7.0, 150 mM NaCl, 50 mM sodium citrate and 15 mM $TbCl_3$). Tb^{3+}-loaded liposomes were then extruded through a 100-nm filter (Whatman Nuclepore). To remove unencapsulated Tb^{3+} and exchange the exterior buffer, the extruded liposomes were subject to gel filtration using a Superose 6 (10/300) column equilibrated with buffer C (20 mM HEPES at pH 7.0, 150 mM NaCl, 50 µM DPA). Liposomes were incubated with GSDMs with or without activating enzyme (En) treatment. GSDMD contained an N-terminal His_6-MBP tag, and a mixture of TEV and 3C at a molar ratio of 1:1 was added, with TEV to remove His_6-MBP and 3C to cleave GSDMD. GSDMA3 contained a SUMO tag, and a mixture of ULP1 and 3C at a molar ratio of 1:1 was added, with ULP1 to remove SUMO and 3C to cleave GSDMA3. In both cases, the molar ratio of lipid:GSDM:En was set to 400:5:2, with GSDM at 0.5 µM. For simplicity, the MBP and SUMO tags are not displayed in the figures. Reactions on 384-well plates (Corning) were monitored by fluorescence (emission 545 nm) using a SpectraMax M5 plate reader (Molecular Devices), with excitation at 274 nm, for 20 min at 2-min intervals.

Pore-dependent cargo release from liposomes

Freshly purified precursor and mature IL-1 proteins were loaded into PS-containing liposomes (25–75% PS, the rest being PC, in the case of GSDMD and GSDMA3 pore formation) or cholesterol-containing liposomes (25% cholesterol + 25% PS + 50% PC, in the case of SLO and PFO pore formation) in a similar fashion to the Tb^{3+} encapsulation procedure, except that buffer A was used throughout and no extrusion was performed. The content of PS or cholesterol was 25% unless otherwise stated in the text or figure legends. Unloaded proteins were removed by repeatedly pelleting the liposomes at 20,000*g* for 15 min in a cold centrifuge and replacing the supernatant with buffer A three times. Differently charged FITC-conjugated dextrans (MW 40 kDa, radii around 40 Å, Sigma Aldrich)—neutral (FD40), CM-modified (53379) and DEAE-modified (01649)—and three other small proteins (MW 12–23 kDa, diameters 30–40 Å)—cyt *c* (C2037, Sigma-Aldrich), CRYGD (AR39126PU-N, OriGene Technologies) and OCM (RPU43138, Biomatik)—were loaded using the same method. The concentrations of the loaded cargoes were approximately 1 µM for proteins and 0.01 mg ml^{-1} (or 0.25 µM) for dextrans. To ensure that cargoes were released through the pores rather than through pore-induced membrane lysis, we used a low sub-lytic concentration (1×) for each pore-forming protein—GSDMD (1× = 0.5 µM), GSDMA3 (1× = 0.5 µM), SLO (1× = 0.1 µM) and PFO (1× = 0.1 µM)—which was evident by the minimal release of encapsulated LDH (CyQUANT LDH Cytotoxicity Kit, Invitrogen) or bulky dextrans (MW 2 MDa, Sigma-Aldrich, FD2000) during a 2-h monitoring period. The molar ratios of MBP-GSDMD:TEV:3C and of SUMO-GSDMA3:ULP1:3C were kept at 5:1:1. The MBP and SUMO tags are not shown in figures for simplicity. No activating enzymes were required for pore formation by SLO and PFO. One aliquot of each reaction was pelleted at time zero, and the pellet was washed three times and dissolved to the original volume with buffer A containing 1% Triton X-100 (Sigma-Aldrich), as a measure of total cargoes loaded into the liposomes. At the indicated time points, the liposomes were pelleted for supernatant collection. For experiments involving IL-1s and the other protein cargoes, the collected supernatants were subject to SDS–PAGE and standard immunoblotting. The primary antibodies were goat polyclonal anti-IL-1β (R&D Systems, AF401NA, 1:500), rabbit polyclonal anti-IL-18 (Genetex, GTX32675, 1:1000), rabbit polyclonal anti-cyt *c* (PA19586, Thermo Fisher Scientific, 1:500), rabbit polyclonal anti-CRYGD (OriGene Technologies, TA332876, 1:500) and rabbit polyclonal anti-OCM (Biomatik, CAU21955, 1:1,000). The incubation conditions for the primary antibodies were 4 °C overnight or room temperature for 1 h. The secondary antibodies were HRP-conjugated anti-goat IgG (Santa Cruz Biotechnology, sc-2354, 1:5,000), anti-rabbit IgG (Cell Signaling Technology, 7074S, 1:5,000) and anti-mouse IgG (Abcam, ab97040, 1:5,000) all used at room temperature for 2 h. The Pierce ECL substrate (Thermo Fisher Scientific) was used for detection. Immunoblots were quantified using ImageJ[41], and IL-1 release rate curves were obtained by fitting hyperbolic functions based on the data points in GraphPad Prism 6. The initial IL-1 release rates were

extrapolated as the derivatives of the fitted functions at time zero. For experiments involving dextrans, the amount of released dextrans in collected supernatants was measured by FITC fluorescence with excitation at 493 nm and emission at 518 nm using a SpectraMax M5 plate reader (Molecular Devices). The maximum fluorescence (100%) was set to the lysed liposomes collected at time zero. Each type of dextran was compared to its own maxima to account for potential variability in FITC labelling.

IL-1 secretion from cells

iBMDMs from wild-type C57BL/6 mice and GSDMD-knockout iBMDMs were supplied by J. Kagan and J. Lieberman (Boston Children's Hospital) and have been authenticated and tested for mycoplasma contamination in previous studies[4,7]. To generate IL-1β-knockout iBMDMs, IL-1β gRNA (5′-CAATGAGTGATACTGCCTGC-3′) was cloned into LentiCRISPR-v2 hygro as previously described[42]. The plasmid was then transfected into HEK293T cells with pSPAX2 and pCMV-VSV-G at a 2:2:1 ratio using the calcium phosphate method. Supernatant collected 2 days later was used to transduce mouse iBMDM cells. After 2 days, hygromycin (300 μg ml^{-1}) was added to select for positive cells for 10 days. Cells were then subcloned in 96-well plates and screened for IL-1β expression by immunoblotting using anti-IL-1β (R&D Systems, AF401NA, 1:500). To express wild-type or charge-mutant GSDMD and A3chim (C-terminally Flag-tagged) in GSDMD-knockout cells and pro-IL-1β in IL-1β-knockout cells, pLVX-puro plasmids containing the respective cDNAs, or without as a control, were transfected into HEK293T cells (Lenti-X Packaging System, Takara Bio). Supernatants were collected after 2 days to transduce knockout iBMDMs. The cells were then subject to selection by puromycin (Sigma, 4 μg ml^{-1}). Expression of GSDMD, A3chim and pro-IL-1β was verified by immunoblotting using anti-GSDMD (Abcam, ab209845, 1:500), anti-Flag (Cell Signaling Technology, 14793S, 1:1,000) and anti-IL-1β (R&D Systems, AF401NA,1:500), respectively. All iBMDMs were maintained in Dulbecco's Modified Eagle's medium (DMEM) with L-glutamine (Thermo Fisher Scientific, 10569-004), supplemented with 10% fetal bovine serum (Thermo Fisher Scientific, 16000-044), at 37 °C with 5% CO_2. For NLRP3 inflammasome activation, iBMDMs were primed with LPS (1 μg ml^{-1}, InvivoGen, tlrl-b5lps) for 4 h. Post priming, glycine (5 mM) treatment was carried out for 1 h before NLRP3 activation using 20 μM nigericin (Sigma-Aldrich, N7143) for 30 min. Alternatively, LPS-primed iBMDMs were treated with 0.5 μM nigericin to allow sustained survival and IL-1β release (12 h) without glycine protection. For SLO- or PFO-mediated IL-1β release, purified SLO or PFO was added to LPS-primed nigericin (20 μM)-stimulated GSDMD-knockout iBMDMs at final concentrations of 0.16 nM or 625 nM for 3 h. In all cases, the supernatant was carefully collected without disturbing the cells. Cell debris was further removed by centrifugation at 21,130*g*, and the clarified supernatant was concentrated using 10,000 MWCO spin columns. Standard immunoblotting after SDS–PAGE was performed to detect precursor or mature IL-1β using anti-IL-1β (AF401NA, R&D Systems, 1:500), with β-actin (Santa Cruz Biotechnology, sc-47778, 1:1,000) as a loading control. Quantification of IL-1β in the supernatant was performed using ELISA (Thermo Fisher Scientific, 88-7013-88). The remaining supernatant and lysate were used to analyse LDH release (CyQUANT LDH Cytotoxicity Assay kit, Invitrogen), with the maximum (100%) set to the LDH level in lysed whole cells.

Mathematical modelling

The electrostatic interaction between the pore and IL-1 was simplified as $E \times q$, in which E is the average electrostatic potential of the pore (kT/e; k is the Boltzmann constant, T the temperature, and e the elementary charge) and q is the net charge of an IL-1 cargo (with unit e). The maximum or initial rate of IL-1 release (r) was approximated as proportional to $\exp[-Eq/(kT)]$. Assumptions of this approximation include that the cargo size is small relative to the pore; that the cargo travels through the pore centre where most flux occurs; and that the electrostatic effect on the cargo is averaged over all directions. According to this relationship, the ratio of the rates (R) between differently charged IL-1 cargoes is $R = \exp[-E\Delta q/(kT)]$, or $\ln(R) = -E\Delta q/(kT)$. A set of measured rate ratios was then plotted against Δq (difference in net charge) to obtain the fitted electrostatic potential E that accounts for the rate differences.

Reporting summary

Further information on research design is available in the Nature Research Reporting Summary linked to this paper.

Data availability

Atomic coordinates of the 33-fold symmetric human GSDMD pore structure have been deposited in the PDB under accession number 6VFE. The cryo-EM density maps of the 33-fold symmetric pore and the prepore have been deposited in the Electron Microscopy Data Bank under accession numbers EMD-21160 and EMD-21161, respectively. All other data are available from the corresponding authors upon reasonable request.

31. Scheres, S. H. RELION: implementation of a Bayesian approach to cryo-EM structure determination. *J. Struct. Biol.* **180**, 519–530 (2012).
32. Zheng, S. Q. et al. MotionCor2: anisotropic correction of beam-induced motion for improved cryo-electron microscopy. *Nat. Methods* **14**, 331–332 (2017).
33. Rohou, A. & Grigorieff, N. CTFFIND4: Fast and accurate defocus estimation from electron micrographs. *J. Struct. Biol.* **192**, 216–221 (2015).
34. Kucukelbir, A., Sigworth, F. J. & Tagare, H. D. Quantifying the local resolution of cryo-EM density maps. *Nat. Methods* **11**, 63–65 (2014).
35. Pettersen, E. F. et al. UCSF Chimera—a visualization system for exploratory research and analysis. *J. Comput. Chem.* **25**, 1605–1612 (2004).
36. Emsley, P. & Cowtan, K. Coot: model-building tools for molecular graphics. *Acta Crystallogr. D* **60**, 2126–2132 (2004).
37. Adams, P. D. et al. PHENIX: a comprehensive Python-based system for macromolecular structure solution. *Acta Crystallogr. D* **66**, 213–221 (2010).
38. Roy, A., Kucukural, A. & Zhang, Y. I-TASSER: a unified platform for automated protein structure and function prediction. *Nat. Protoc.* **5**, 725–738 (2010).
39. Baker, N. A., Sept, D., Joseph, S., Holst, M. J. & McCammon, J. A. Electrostatics of nanosystems: application to microtubules and the ribosome. *Proc. Natl Acad. Sci. USA* **98**, 10037–10041 (2001).
40. Xia, S., Ruan, J. & Wu, H. Monitoring gasdermin pore formation in vitro. *Methods Enzymol.* **625**, 95–107 (2019).
41. Schneider, C. A., Rasband, W. S. & Eliceiri, K. W. NIH Image to ImageJ: 25 years of image analysis. *Nat. Methods* **9**, 671–675 (2012).
42. Sanjana, N. E., Shalem, O. & Zhang, F. Improved vectors and genome-wide libraries for CRISPR screening. *Nat. Methods* **11**, 783–784 (2014).

Acknowledgements We thank B. Honig, T. Rapoport, F. Shao, J. Kagan, D. Golenbock, S. Blacklow, A. Kruse and M. Liao for discussions. For structural data collection, we thank R. Walsh, S. Sterling, S. Rawson and Z. Li at the Harvard Cryo-EM Center for Structural Biology and K. Song, K. Lee and C. Xu at the Cryo-EM Core Facility at University of Massachusetts Medical School. This work was supported by US National Institutes of Health grants R01AI139914 (H.W. and J.L.), DP1HD087988 (H.W.), R01AI124491 (H.W.), R01CA240955 (J.L.), R01DK095045 (A.G.), R01DK099465 (A.G.) and 5T32HL066987-18 (T.-M.F.). S.X. received an Albert J. Ryan fellowship. J.R. and Z.Z. received postdoctoral fellowships from the Charles A. King Trust.

Author contributions H.W., J.R. and S.X. conceived the study. S.X. and J.R. reconstituted and optimized GSDMD assemblies and determined the cryo-EM structures. S.X., Z.Z. and V.G.M. performed cellular experiments. S.X., J.L.P., Y.D., S.M.V., L.W. and T.-M.F. performed biochemical experiments. H.W., J.L., A.G. and M.P.J. supervised the project. All authors organized and analysed data. H.W. and S.X. wrote the paper with input from all authors.

Competing interests H.W. and J.L. are co-founders of Ventus Therapeutics. The other authors declare no competing interests.

Additional information

Supplementary information The online version contains supplementary material available at https://doi.org/10.1038/s41586-021-03478-3.

Correspondence and requests for materials should be addressed to J.R. or H.W.

Peer review information *Nature* thanks Helen Saibil and the other, anonymous, reviewer(s) for their contribution to the peer review of this work. Peer reviewer reports are available.

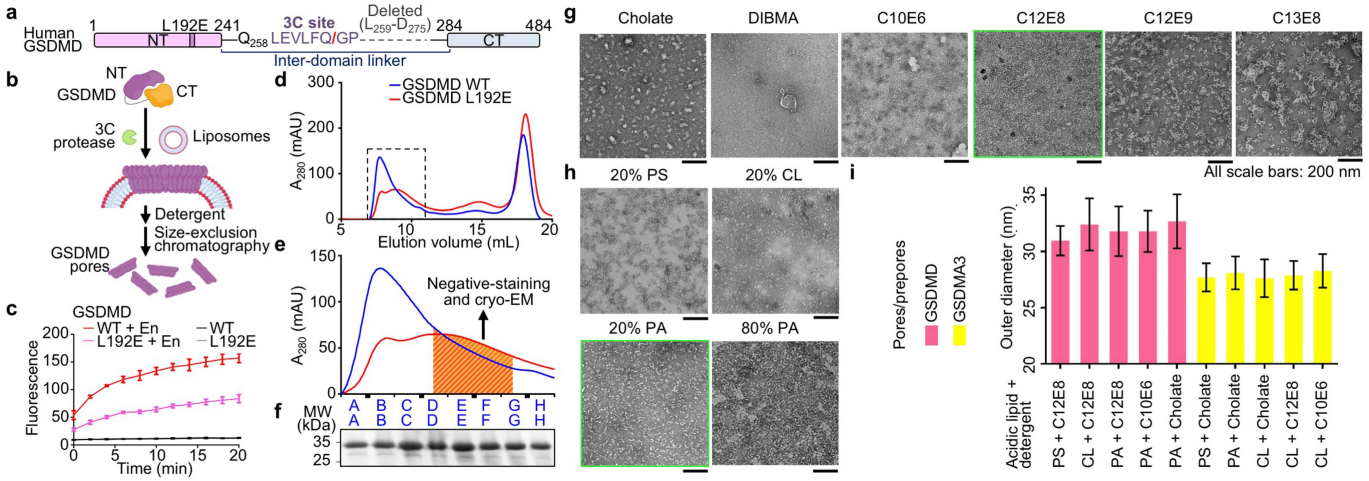

Extended Data Fig. 1 | Reconstitution and purification of GSDMD assemblies. a, Optimized construct for human GSDMD, referred to as wild-type (WT) GSDMD for convenience. The N-terminal MBP tag and the TEV-cleavable linker between MBP and GSDMD-NT are not shown. **b**, Schematic of GSDMD pore and prepore reconstitution. **c**, Reduced, but not abolished, activity of the GSDMD(L192E) mutant shown by Tb^{3+} leakage assay ($n = 3$ biological replicates). En, activating enzyme. **d**, **e**, Size-exclusion chromatography profiles (**d**) and an enlargement of the boxed region (**e**). The box encloses the fractions containing the majority of wild-type GSDMD or GSDMD(L192E) assemblies. The shaded fractions containing well-dispersed particles (**e**) were used for electron microscopy data collection. **f**, SDS–PAGE showing wild-type GSDMD-NT at around 30 kDa from the corresponding fractions in **e**. **g**, Detergent screen. A group of non-ionic detergents with commercial shorthand C_xE_y (C_x, x number of carbons in the alkyl chain; E_y, y number of ethylene glycol repeats) yielded stable GSDMD pores. $C_{12}E_8$ was chosen as the final solubilizing agent. Scale bars, 200 nm. **h**, GSDMD pores extracted by 1% $C_{12}E_8$ from liposomes containing different types and amounts (%) of acidic lipids. Liposomes containing 20% PA were chosen. Scale bars, 200 nm. **i**, Sizes of GSDMD and GSDMA3 assemblies reconstituted on liposomes containing different acidic lipids (20%) and extracted by different types of detergent (1% C_xE_y, or 50 mM cholate), shown by outer diameters measured under negative-stain electron microscopy (from left to right, $n = 64$, 42, 77, 73, 14, 34, 45, 23, 21 and 18 particles). Data shown in **c** and **i** are mean ± s.d. Data shown in **f**–**h** are representative of three independent experiments.

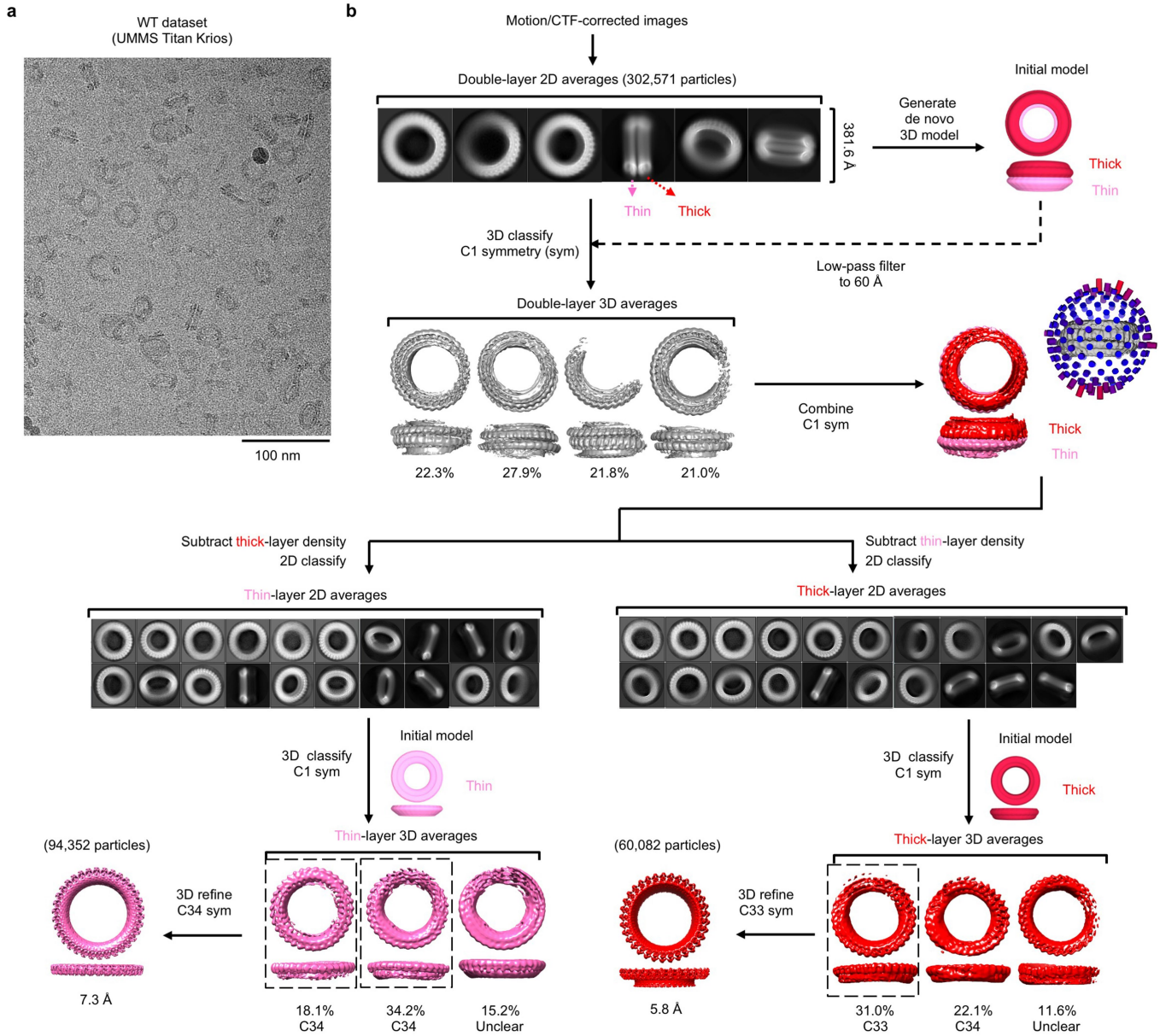

Extended Data Fig. 2 | Cryo-EM data processing for the wild-type GSDMD dataset. a, A cryo-EM image of the wild-type GSDMD sample. Data are representative of three independent experiments. Scale bar, 100 nm. **b**, Processing of the wild-type GSDMD cryo-EM dataset. Initial 2D classes showed a ring-stacking phenomenon, which added to structural heterogeneity and posed challenges for symmetry determination. Density subtraction was therefore performed, followed by 3D reconstruction of each ring without assumption of symmetry, after which particle symmetry could be determined for certain 3D classes. These classes were then refined with their respective symmetry imposed to yield final cryo-EM maps.

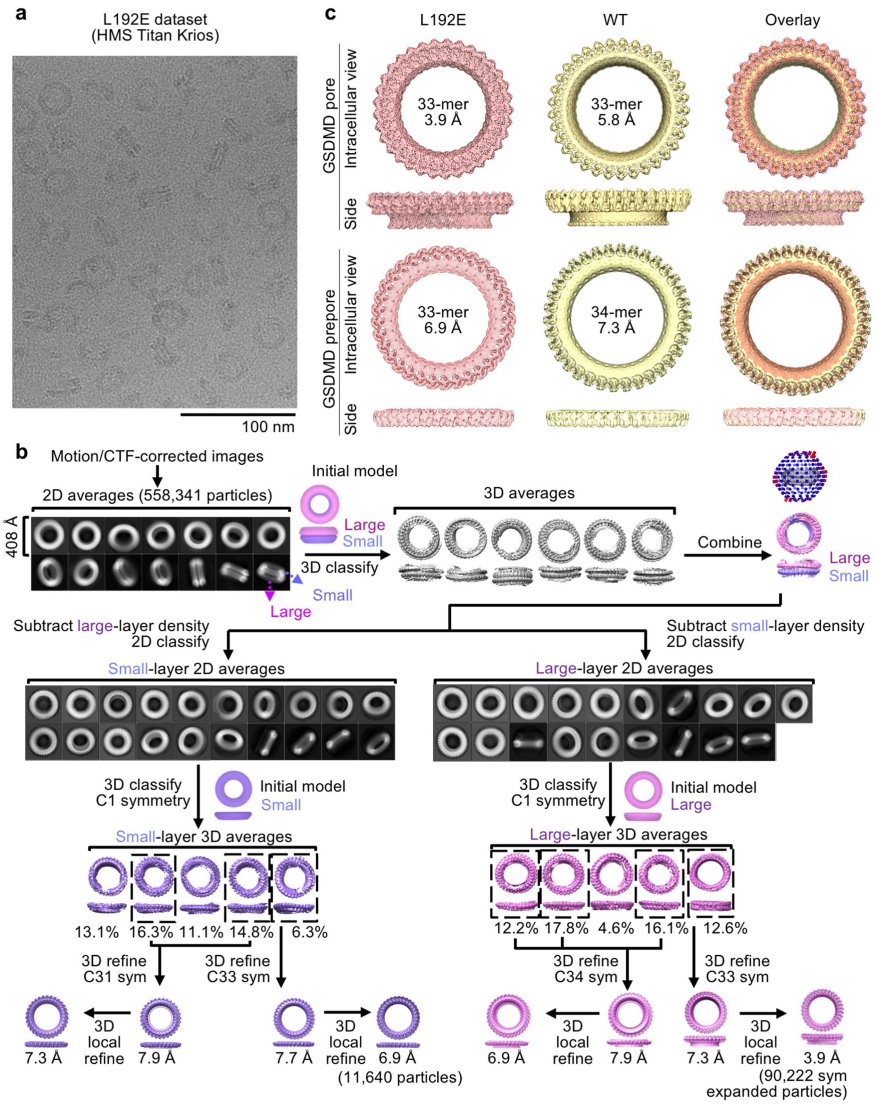

Extended Data Fig. 3 | Cryo-EM data processing for the GSDMD(L192E) dataset. a, A cryo-EM image of the GSDMD(L192E) sample. Data are representative of three independent experiments. Scale bar, 100 nm. **b**, Processing of the GSDMD(L192E) cryo-EM dataset. This dataset was first processed following the procedures for the wild-type dataset. Cryo-EM maps obtained from 3D refinement with symmetry imposed were further classified without alignment to remove heterogeneous particles. Then, the best 3D classes were refined again to improve resolutions. A 3D reconstruction at 7.3 Å was further improved by symmetry expansion, 3D classification without alignment, 3D local refinement, and per-particle CTF refinement to reach the final map at 3.9 Å resolution. **c**, Similarity of cryo-EM maps generated from the wild-type and L192E datasets. Owing to the higher resolutions, maps from the L192E dataset were chosen for model building.

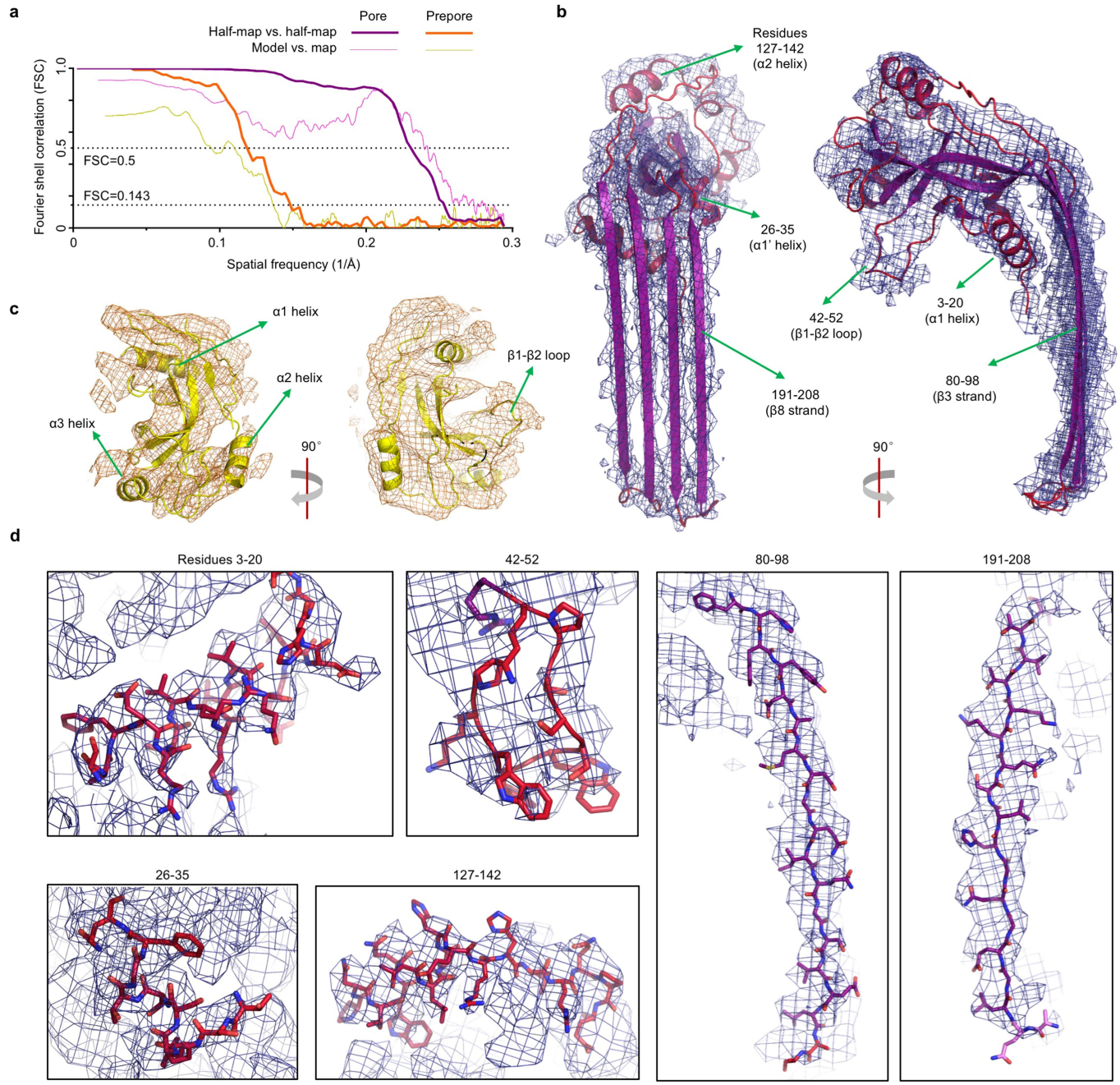

Extended Data Fig. 4 | Analysis of cryo-EM densities and models. **a**, Half-map-to-half-map and model-to-map FSC for the 33-fold symmetric GSDMD pore and prepore from the L192E dataset. Horizontal dashed lines represent FSC cut-offs at 0.5 and 0.143. **b**, **c**, Pore-form (**b**) and prepore-form (**c**) GSDMD subunits fitted into their respective cryo-EM density. Arrows indicate secondary structural elements specified by residue numbers. **d**, Close-up views of the pore-form GSDMD structure fitted into its cryo-EM density at six representative locations denoted by residue numbers.

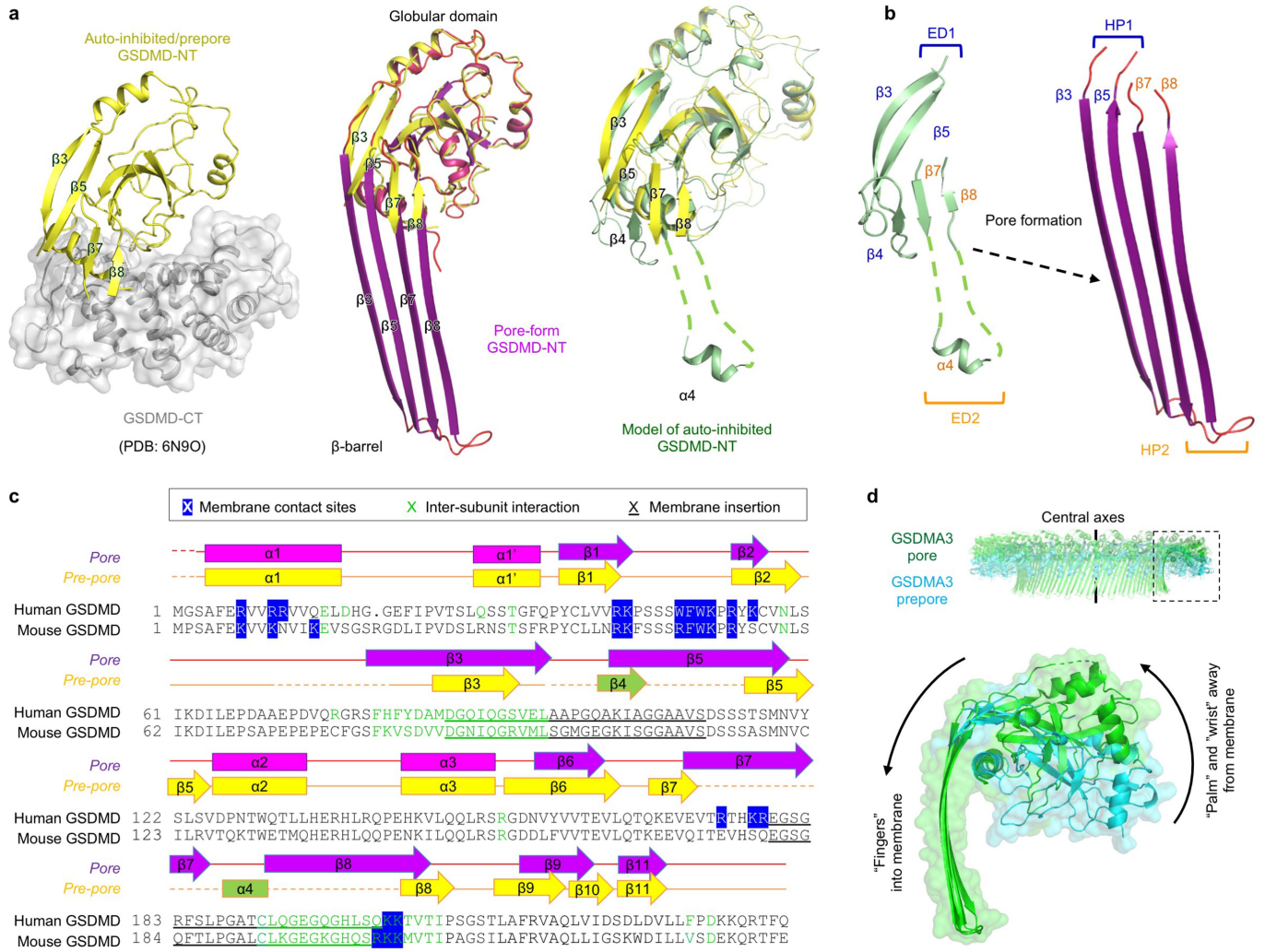

Extended Data Fig. 5 | β-hairpin extension and prepore-to-pore transition. **a**, Comparison between autoinhibited, prepore-form and pore-form GSDMD. The autoinhibited GSDMD-NT was obtained from the crystal structure of full-length GSDMD (PDB: 6N9O). The β4 strand and α4 helix are invisible in the crystal structure and were modelled on the basis of the crystal structure of full-length GSDMA3 (PDB: 5B5R). **b**, Formation of β-hairpins. The β3–β4–β5 region constitutes the first extension domain (ED1), which transforms into hairpin (HP) 1 by refolding. The β7–α4–β8 region represents ED2 and becomes HP2. **c**, Sequence alignment of human and mouse GSDMD, with secondary structures and key residues denoted. Blue highlighting indicates residues responsible for lipid binding, through either hydrophobic or charged interactions; green highlighting indicates residues at inter-subunit interfaces; and underlining indicates residues that are important for membrane insertion. **d**, Conserved rigid-body movement of the globular domain ('palm') towards the membrane-distal direction during GSDM pore formation, shown by alignment of the GSDMA3 pore structure (PDB: 6CB8) and prepore model at their central axes.

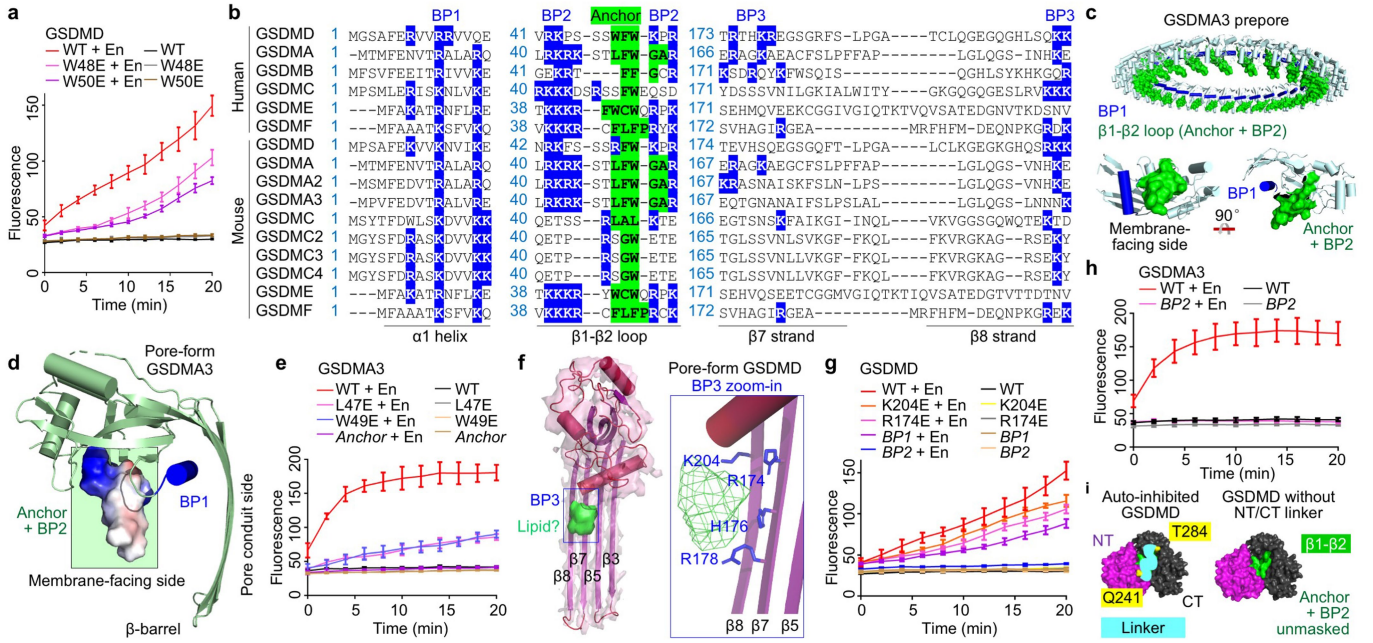

Extended Data Fig. 6 | Hydrophobic anchor and basic patches of GSDMs. **a**, Effects of mutations in the hydrophobic anchor on GSDMD pore formation assessed by Tb^{3+} leakage from liposomes ($n = 3$ biological replicates). **b**, GSDM sequences aligned at the hydrophobic anchor and BPs. Blue highlighting indicates basic residues at BPs; green highlighting indicates hydrophobic residues of the anchor; and dashes indicate gaps. **c**, The GSDMA3 prepore model with the β1–β2 loop highlighted in green and BP1 shown in blue. A GSDMA3 prepore subunit is also shown in two orientations. **d**, A side view of pore-form GSDMA3 (PDB: 6CB8), with electrostatic surface shown around the β1–β2 loop. The anchor and BP2 are boxed in green. **e**, Impairment of the pore-forming ability of GSDMA3 by mutations in the hydrophobic anchor, shown by Tb^{3+} leakage assay ($n = 3$ biological replicates). 'Anchor' indicates that L47, F48 and W49 are mutated to E. **f**, A cryo-EM density blob that probably represents heads of phospholipids near BP3. Basic residues in BP3 point towards the blob. **g**, Effects of mutations in BP1 (R7, R10 and R11 mutated to E), BP2 (R42, K43, K51 and R53 mutated to E) and BP3 (K204 or R174 mutated to E) on GSDMD activity evaluated by Tb^{3+} leakage assay ($n = 3$ biological replicates). **h**, Importance of BP2 for GSDMA3 pore formation, shown by Tb^{3+} leakage assay ($n = 3$ biological replicates). Here, in BP2, R41, K42, R43 and K44 are mutated to E. **i**, Exposure of the hydrophobic anchor and BP2 upon removal of the inter-domain linker between GSDMD-NT and GSDMD-CT. Surface representations are shown for autoinhibited GSDMD (PDB: 6N9O) with and without the inferred linker (cyan curve connecting Q241 and T284). Purple, GSDMD-NT; black: GSDMD-CT; green, anchor–BP2 region; yellow, two ends of the linker. Data shown in **a**, **e**, **g** and **h** are mean ± s.d.

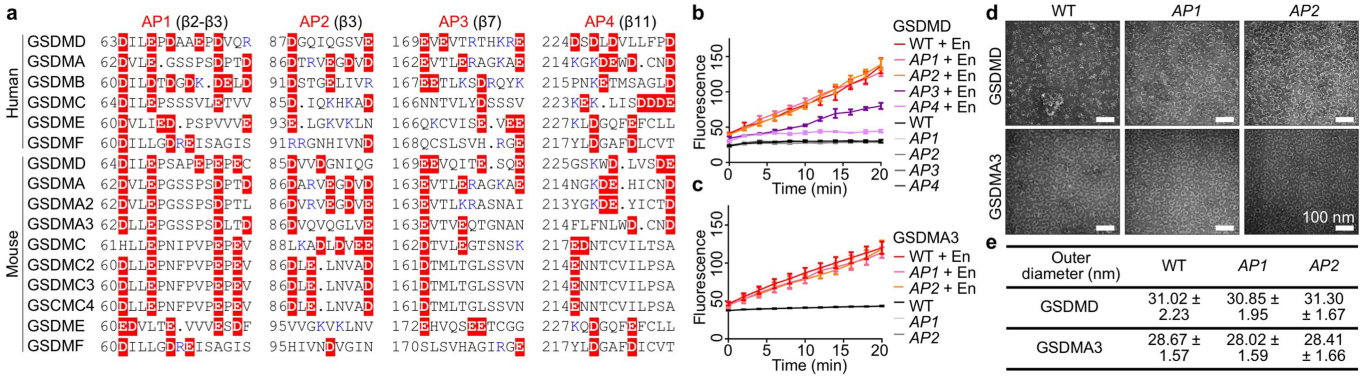

Extended Data Fig. 7 | GSDM acidic patches and their mutations.
a, Locations of APs shown by aligned GSDM sequences. Dots, strings of omitted uncharged residues; red highlighting, acidic residues; blue, basic residues. Of note, the basic residues near the APs may face the membrane (such as those in BP3) and therefore do not necessarily weaken the acidity of the pore conduit. **b**, Assessment of alanine mutations of GSDMD APs 1–4 by Tb^{3+} leakage assay ($n = 3$ biological replicates). **c**, Assessment of alanine mutations of GSDMA3 AP1 and AP2 by Tb^{3+} liposome leakage assay ($n = 3$ biological replicates). **d**, Negative-staining electron microscopy images of wild-type and AP-mutant GSDMD and GSDMA3 assemblies, solubilized from liposomes using $C_{12}E_8$ and cholate, respectively. Data shown are representative of three independent experiments. Scale bars, 100 nm. **e**, Outer diameters of wild-type or AP-mutant GSDMD and GSDMA3 assemblies, measured under negative-staining electron microscopy ($n = 50$ particles per group). Data shown in **b**, **c** and **e** are mean ± s.d.

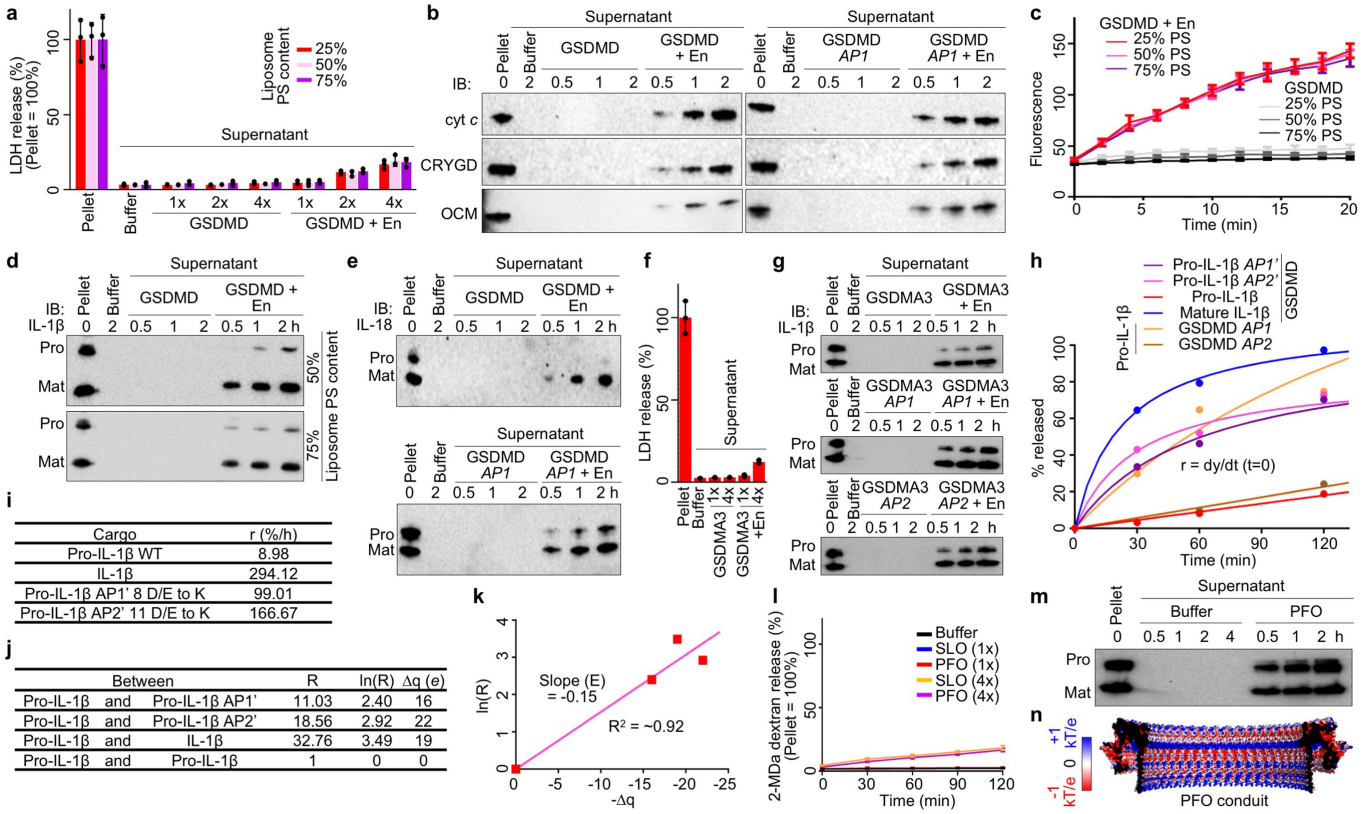

Extended Data Fig. 8 | Liposome experiments and electrostatics analysis. **a**, Unlysed liposomes (25–75% PS) demonstrate that LDH release is minimal when GSDMD is added at a sub-lytic concentration (1× = 0.5 μM) ($n = 3$ biological replicates). **b**, Release of cyt *c*, CRYGD and OCM from liposomes permeabilized by GSDMD shown by immunoblotting. **c**, Similar rates of GSDMD pore formation on liposomes of various acidic lipid contents (25–75% PS), according to Tb^{3+} release assay ($n = 3$ biological replicates). **d**, Preferential IL-1β release from liposomes (50% and 75% PS) perforated by GSDMD shown by immunoblotting. **e**, Release of pro-IL-18 and IL-18 from liposomes permeabilized by GSDMD shown by immunoblotting. **f**, Minimal LDH release when GSDMA3 was activated at a sub-lytic concentration (1× = 0.5 μM) ($n = 3$ biological replicates), demonstrating that the liposomes are intact. **g**, Release of pro-IL-1β and mature IL-1β from liposomes perforated by GSDMA3 shown by immunoblotting. **h**, Release rates of IL-1β cargoes through GSDMD pores shown by fitted hyperbolic functions. **i**, Initial release rates (*r*) extrapolated from **h**. **j**, Charge differences among the cargoes (Δ*q*) and rate ratios (*R*). **k**, Plot of ln(*R*) against Δ*q* to estimate the electrostatic potential (*E*) of the GSDMD pore conduit. **l**, A lack of release of encapsulated bulky FITC-labelled dextrans (2 MDa) when SLO or PFO was added at a sub-lytic concentration (1× = 0.1 μM) ($n = 3$ biological replicates), demonstrating that the liposomes are intact. **m**, Similar release of pro-IL-1β and mature IL-1β from liposomes permeabilized by PFO. **n**, Electrostatic surfaces of the modelled PFO pore conduit. Data shown in **a**, **c**, **f** and **l** are mean ± s.d. Data are representative of three (**b**) or two (**d**, **e**, **g**, **m**) independent experiments.

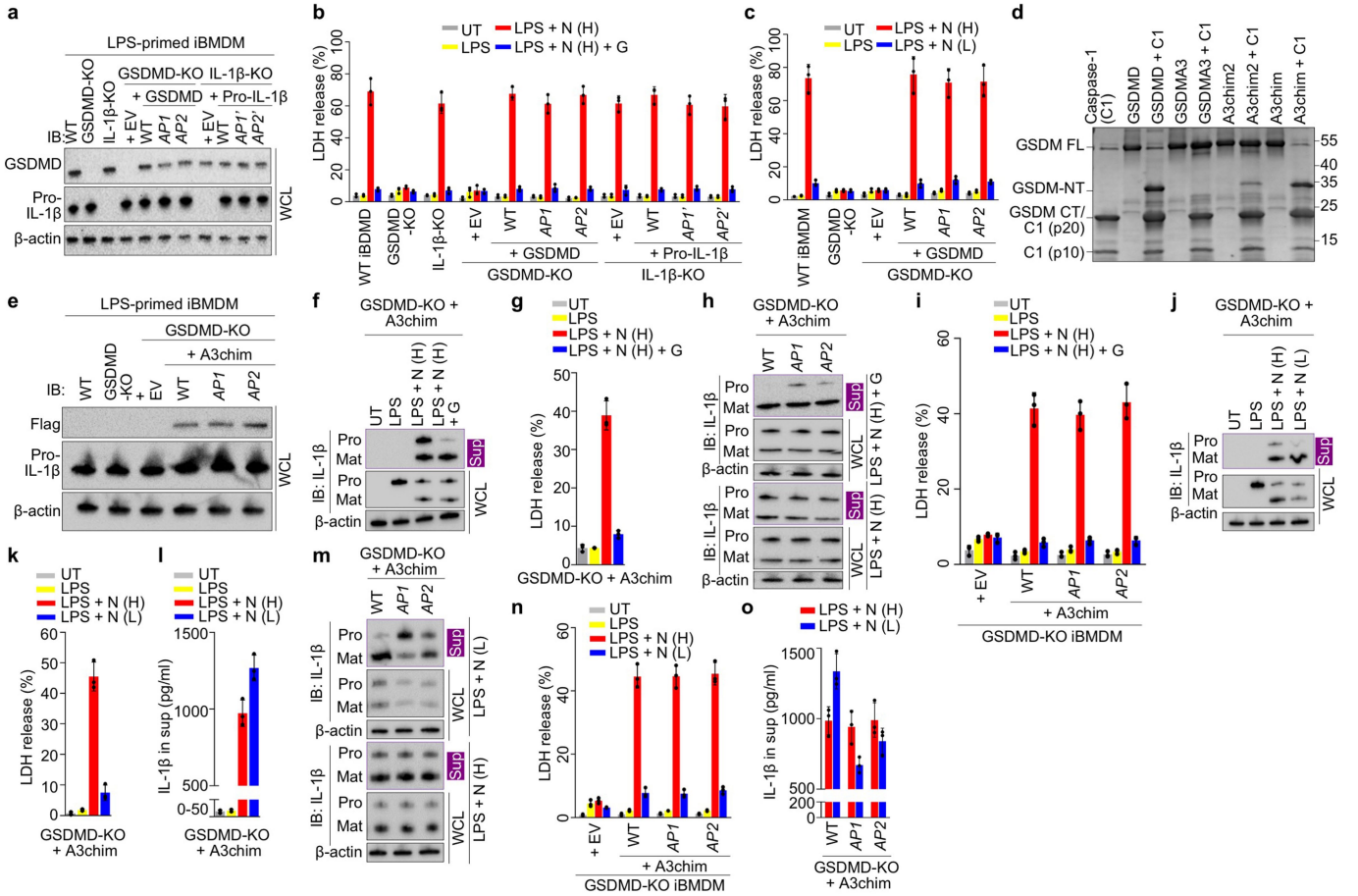

Extended Data Fig. 9 | Macrophage experiments. a, Comparable expression of wild-type and charge-mutant GSDMD in GSDMD-knockout iBMDMs, and of wild-type and charge-mutant pro-IL-1β in IL-1β-knockout iBMDMs, shown by immunoblotting. **b**, **c**, Similar sensitivity of knockout iBMDMs reconstituted with wild-type or charge-mutant GSDMD or pro-IL-1β to pyroptosis and death evasion by glycine protection (**b**) or low-dose nigericin treatment (**c**), shown by LDH release ($n = 3$ biological replicates). **d**, Cleavage of engineered GSDMA3 chimera (A3chim) by caspase-1 (C1), shown by SDS–PAGE of proteolysis reactions using purified proteins. **e**, Comparable expression of A3chim (Flag-tagged) and its AP mutants in GSDMD-knockout cells. AP1, 4 D/E to A; AP2, 2 D/E to A. **f**, **g**, Preferential release of mature IL-1β from glycine-protected living iBMDMs permeabilized by A3chim, shown by immunoblotting (**f**) and LDH release ($n = 3$ biological replicates) (**g**). **h**, **i**, IL-1β release from GSDMD-knockout iBMDMs expressing wild-type or AP-mutant A3chim under glycine protection, shown by immunoblotting (**h**) and LDH release ($n = 3$ biological replicates) (**i**). **j**–**l**, IL-1β release from living GSDMD-knockout iBMDMs expressing A3chim stimulated by low-dose nigericin, characterized by immunoblotting (**j**), LDH release ($n = 3$ biological replicates) (**k**) and ELISA ($n = 3$ biological replicates) (**l**). **m**, **n**, IL-1β release from low-dose nigericin-stimulated GSDMD-knockout iBMDMs expressing wild-type or AP-mutant A3chim, evaluated by immunoblotting (**m**), LDH release ($n = 3$ biological replicates) (**n**) and ELISA ($n = 3$ biological replicates) (**o**). Data shown in **b**, **c**, **g**, **i**, **k**, **l**, **n** and **o** are mean ± s.d. Data shown in **a**, **d**–**f**, **h**, **j** and **m** are representative of two independent experiments.

Extended Data Table 1 | Cryo-EM data collection, refinement and validation statistics

	WT pore	WT prepore	L192E pore (EMDB-21160) (PDB 6VFE)	L192E prepore (EMDB-21161)
Data collection and processing				
Magnification	81,000	81,000	105,000	105,000
Voltage (kV)	300	300	300	300
Electron exposure (e–/Å^2)	48.58	48.58	63.25	63.25
Defocus range (μm)	-1.0 to -2.5	-1.0 to -2.5	-0.8 to -2.5	-0.8 to -2.5
Pixel size (Å)	0.53	0.53	0.85	0.85
Symmetry imposed	C33	C34	C33	C33
Initial particle images (no.)	60,082	94,352	41,413	21,200
Final particle images (no.)	60,082	94,352	2,734	11,640
Map resolution (Å)	5.8	7.3	3.9	6.9
FSC threshold	0.143	0.143	0.143	0.143
Map resolution range (Å)	60.0-5.8	60.0-7.3	60.0-3.9	60.0-6.9
Refinement				
Initial model used (PDB code)			6N9O	6N9O
Model resolution (Å)			3.7/4.2	7.3/10.6
FSC threshold			0.143/0.5	0.143/0.5
Model resolution range (Å)			59.0-3.4	45.9-3.4
Map sharpening *B* factor (Å^2)			-168.81	-652.00
Model composition				
Non-hydrogen atoms			62,238	46,299
Protein residues			7,953	5,742
Ligands			0	0
B factors (Å^2)				
Protein			73.57	215.68
Ligand			N/A	N/A
R.m.s. deviations				
Bond lengths (Å)			0.007	0.005
Bond angles (°)			0.943	1.153
Validation				
MolProbity score			2.81	3.00
Clashscore			6.96	26.07
Poor rotamers (%)			6.76	4.32
Ramachandran plot				
Favored (%)			89.82	87.35
Allowed (%)			10.18	12.65
Disallowed (%)			0.00	0.00

nature research

Corresponding author(s): Hao Wu, Jianbin Ruan

Last updated by author(s): Mar 15, 2021

Reporting Summary

Nature Research wishes to improve the reproducibility of the work that we publish. This form provides structure for consistency and transparency in reporting. For further information on Nature Research policies, see Authors & Referees and the Editorial Policy Checklist.

Statistics

For all statistical analyses, confirm that the following items are present in the figure legend, table legend, main text, or Methods section.

n/a	Confirmed
☐	☒ The exact sample size (*n*) for each experimental group/condition, given as a discrete number and unit of measurement
☐	☒ A statement on whether measurements were taken from distinct samples or whether the same sample was measured repeatedly
☒	☐ The statistical test(s) used AND whether they are one- or two-sided *Only common tests should be described solely by name; describe more complex techniques in the Methods section.*
☒	☐ A description of all covariates tested
☒	☐ A description of any assumptions or corrections, such as tests of normality and adjustment for multiple comparisons
☐	☒ A full description of the statistical parameters including central tendency (e.g. means) or other basic estimates (e.g. regression coefficient) AND variation (e.g. standard deviation) or associated estimates of uncertainty (e.g. confidence intervals)
☒	☐ For null hypothesis testing, the test statistic (e.g. *F*, *t*, *r*) with confidence intervals, effect sizes, degrees of freedom and *P* value noted *Give P values as exact values whenever suitable.*
☒	☐ For Bayesian analysis, information on the choice of priors and Markov chain Monte Carlo settings
☒	☐ For hierarchical and complex designs, identification of the appropriate level for tests and full reporting of outcomes
☒	☐ Estimates of effect sizes (e.g. Cohen's *d*, Pearson's *r*), indicating how they were calculated

Our web collection on statistics for biologists contains articles on many of the points above.

Software and code

Policy information about availability of computer code

Data collection	Cryo-EM data collection: SerialEM (version 3.6).
Data analysis	Cryo-EM data analysis: MotionCor2 (version 1.1.0), CTFFIND4 (version 4.1), Relion (version 3.0), Coot (version 0.8.9), PHENIX (version 1.17.1), and ResMap (version 1.9). Stuctural modelling: I-TASSER (version 5.1) and SWISS-MODEL (accessed through the EXPASY server). Sequence alignment: Clustal Omega (accessed through the EMBL-EBI server). Molecular Graphics: UCSF Chimera (version 1.13.1) and PyMOL (version 2.3.1). Immunoblot quantification: ImageJ (version 1.51). Data plotting: GraphPad Prism (version 8).

For manuscripts utilizing custom algorithms or software that are central to the research but not yet described in published literature, software must be made available to editors/reviewers. We strongly encourage code deposition in a community repository (e.g. GitHub). See the Nature Research guidelines for submitting code & software for further information.

Data

Policy information about availability of data

All manuscripts must include a data availability statement. This statement should provide the following information, where applicable:

- Accession codes, unique identifiers, or web links for publicly available datasets
- A list of figures that have associated raw data
- A description of any restrictions on data availability

Atomic coordinates of the 33-fold symmetric human GSDMD pore structure have been deposited in the Protein Data Bank (PDB) under accession number 6VFE. The cryo-EM density maps of the 33-fold symmetric pore and the pre-pore have been deposited in the Electron Microscopy Data Bank (EMDB) under accession numbers 21160 and 21161, respectively. All other data are available from the corresponding authors upon reasonable request. Several structural coordinates in the PDB database were used in this study, which can be located by accession numbers 6CB8, 5B5R, 6N9O, 9ILB, 3WO2, 5LY6, 2B4Z, 1H4A, and 1TTX.

Field-specific reporting

Please select the one below that is the best fit for your research. If you are not sure, read the appropriate sections before making your selection.

☒ Life sciences ☐ Behavioural & social sciences ☐ Ecological, evolutionary & environmental sciences

For a reference copy of the document with all sections, see nature.com/documents/nr-reporting-summary-flat.pdf

Life sciences study design

All studies must disclose on these points even when the disclosure is negative.

Sample size	Sample sizes were not pre-determined. Cryo-EM images were collected until structures of satisfactory quality were solved, which suggested sufficient sample size. For biochemical and cellular experiments, no information was derived about a population based on sampling, and therefore sample size determination was not necessary.
Data exclusions	In cryo-EM processing, we discarded "junk" particles that could not be classified into useful 3D reconstructions. This is a widely used and accepted practice in the cryo-EM field. No other data were excluded from analysis.
Replication	All experiments were performed independently at least two or three times with similar results, as described in the figure legends.
Randomization	Proteins, liposomes, and cells were randomly allocated to the wells in each experimental group. Other randomization of experimental groups was not relevant to this study, and independent variables were controlled and did not require randomization.
Blinding	Blinding was not performed as subjective analysis was not needed. Each experiment was analyzed using consistent methods. Random allocation and quantitative measurements using various approaches and reaction kits as described in the methods minimized biased assessments.

Reporting for specific materials, systems and methods

We require information from authors about some types of materials, experimental systems and methods used in many studies. Here, indicate whether each material, system or method listed is relevant to your study. If you are not sure if a list item applies to your research, read the appropriate section before selecting a response.

Materials & experimental systems

n/a	Involved in the study
☐	☒ Antibodies
☐	☒ Eukaryotic cell lines
☒	☐ Palaeontology
☒	☐ Animals and other organisms
☒	☐ Human research participants
☒	☐ Clinical data

Methods

n/a	Involved in the study
☒	☐ ChIP-seq
☒	☐ Flow cytometry
☒	☐ MRI-based neuroimaging

Antibodies

Antibodies used	Anti-IL-1β (R&D Systems, AF401NA, Lot: NP2816021, 1:500) Anti-IL-18 (Genetex, GTX32675, 1:1000) Anti-CYC (Thermo Fisher Scientific, PA19586, 1:500) Anti-CRYGD (OriGene Technologies, TA332876, Lot: 0017090201, 1:500) Anti-OCM (Biomatik, CAU21955, 1:1000) Anti-GSDMD (Abcam, ab209845, Lot: GR3205112-21, 1:500) Anti-Flag (Cell Signaling Technology, 14793S, Lot: 5, 1:1000) Anti-β-actin (Santa Cruz Biotechnology, sc-47778, Lot: C1620, 1:1000) HRP-conjugated anti-goat IgG (Santa Cruz Biotechnology, sc-2354, Lot: H1720, 1:5000) HRP-conjugated anti-rabbit IgG (Cell Signaling Technology, 7074S, Lot: 28; 1:5000) HRP-conjugated anti-mouse IgG (Abcam, ab97040, Lot: GR3255988-5, 1:5000)
Validation	All antibodies used in this study are commercially available and have been validated by the manufacturers' and/or previous publications. Anti-IL-1β (https://www.rndsystems.com/products/mouse-il-1beta-il-1f2-antibody_af-401-na; PMID: 26968342, 27667687, 28636953, 28666573, 28892569, 28943355, 29195811, 29249358, 29290574, 29343442, 29414684, 29719235, 29735414, 29937272, 29937375, 29958799, 30157429, 30212649, 30314759, 30366764, 30463019, 30485804, 31085177, 31350176, 31420217, 31693761, 32096759) Anti-IL-18 (https://www.genetex.com/Product/Detail/IL18-antibody/GTX32675; PMID: 33248263) Anti-CYC (https://www.thermofisher.com/antibody/product/Cytochrome-C-Antibody-Polyclonal/PA1-9586; PMID: 26620075)

Anti-CRYGD (https://www.origene.com/catalog/antibodies/primary-antibodies/ta332876/crygd-rabbit-polyclonal-antibody)
Anti-OCM (https://www.biomatik.com/antibodies/oncomodulin-ocm-polyclonal-antibody-cat-cau21955/)
Anti-GSDMD (https://www.abcam.com/gsdmd-antibody-epr19828-ab209845.html; PMID: 31097341, 31311035)
Anti-Flag (https://www.cellsignal.com/products/primary-antibodies/dykddddk-tag-d6w5b-rabbit-mab-binds-to-same-epitope-as-sigma-s-anti-flag-m2-antibody/14793; PMID: 27379371, 27727322, 29033361, 29056322, 29244109, 29576536, 29617643, 29622465, 29861175, 29920279, 30057310, 30078703, 30118680, 30184489, 30699353, 30893587, 31031140, 31056462, 31327703, 31390677, 31416967, 31433977, 31665626, 31693890, 31775033, 31881009, 31882361, 32023459, 32420875)
Anti-β-actin (https://www.scbt.com/p/beta-actin-antibody-c4; PMID: 20808797, 23798596, 23970784, 24248461, 24424059, 24823391, 24877629, 25057792, 25488013, 25562615, 25635620, 26181104, 26393301, 26562261, 26824363, 26943364, 26990063, 27035653, 27393691, 27453575, 27555288, 27754789, 27967217, 27967242, 28005008, 28017544, 28132844, 28137966, 28196867)
HRP-conjugated anti-goat IgG (https://www.scbt.com/p/mouse-anti-goat-igg-hrp; PMID: 29897336, 30053437, 30062776, 30304388, 31031143, 31056282, 31533030, 31658360, 31715027, 31811660, 31883376, 32286230, 32701054)
HRP-conjugated anti-rabbit IgG (https://www.cellsignal.com/products/wb-ip-reagents/phototope-hrp-western-blot-detection-system-anti-rabbit-igg-hrp-linked-antibody/7074.html?bvstate=pg:2/ct:r; PMID: 23970788, 24140712, 24828612, 25378159, 25546454, 25574706, 25957629, 26335297, 26451739, 26881311, 26919384, 27007072, 27254006, 27309940, 27333032, 27338714, 27575030, 27700985, 27715254, 27912057, 28100394, 28105751, 28214337, 28343940)
HRP-conjugated anti-mouse IgG (https://www.abcam.com/goat-mouse-igg-hl-hrp-preadsorbed-ab97040.html; PMID: 27644592, 28606780, 29750970)

Eukaryotic cell lines

Policy information about cell lines

Cell line source(s)	HEK293T cells were obtained from American Type Culture Collection (ATCC). iBMDM cells from WT C57BL/6 mice and GSDMD-KO iBMDMs were supplied by Judy Lieberman's and Jonathan Kagan's labs (Boston Children's Hospital). IL-1beta-KO iBMDMs were generated using CRISPR as detailed in Methods. Reconstituted iBMDMs of KO bacgrounds were generated following standard lentiviral transduction as detailed in Methods.
Authentication	HEK293T cells were authenticated by ATCC. WT iBMDMs and GSDMD-KO iBMDMs from Lieberman's and Kagan's labs have been authenticated previously (Liu et al., Nature 2016, DOI: 10.1038/nature18629; Evavold et al., Immunity 2018, DOI: 10.1016/j.immuni.2017.11.013). IL-1beta-KO iBMDMs were obtained by CRISPR and verified by immunoblotting as detailed in Methods. All cells were frequently checked by their morphological features and functions (including responsiveness to inflammasome activation, IL-1 release, and pyroptosis). No other authentication was performed.
Mycoplasma contamination	All cell lines were tested to be mycoplasma-negative by PCR.
Commonly misidentified lines (See ICLAC register)	No commonly misidentified cell lines were used in this study.